ornl

ORNL/TM-10792

OAK RIDGE
NATIONAL
LABORATORY

MARTIN MARIETTA

Alpha-Particle Losses in Compact Torsatron Reactors

S. L. Painter
J. F. Lyon

OPERATED BY
MARTIN MARIETTA ENERGY SYSTEMS, INC.
FOR THE UNITED STATES
DEPARTMENT OF ENERGY

Printed in the United States of America. Available from
National Technical Information Service
U.S. Department of Commerce
5285 Port Royal Road, Springfield, Virginia 22161
NTIS price codes—Printed Copy: A04; Microfiche A01

ORNL/TM-10792
Dist. Category UC-421, 424, 426, 427

Fusion Energy Division

ALPHA-PARTICLE LOSSES IN COMPACT TORSATRON REACTORS

S. L. Painter
J. F. Lyon

Date published—October 1988

Prepared by the
OAK RIDGE NATIONAL LABORATORY
Oak Ridge, Tennessee 37831
operated by
MARTIN MARIETTA ENERGY SYSTEMS, INC.
for the
U.S. DEPARTMENT OF ENERGY
under contract DE-AC05-84OR21400

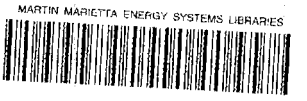

CONTENTS

ABSTRACT

Loss of alpha particles from compact torsatron reactors with $M = 6$, 9, and 12, where M is the number of field periods, is studied. The direct loss is a relatively get weak function of radius and energy and varies from $\simeq$33% for $M = 6$ to $\simeq$18% for $M = 12$. Loss of alpha particles through scattering into the loss region is calculated using the Fokker-Planck equation and found to contribute an additional alpha-particle energy loss of $\simeq$15%. The consequences of these relatively large losses for torsatron reactor design are discussed. A figure of merit that characterizes the orbit confinement for a magnetic configuration is deduced and used to show how the direct alpha-particle losses might be reduced.

I. INTRODUCTION

The development of compact torsatron configurations[1] with low to moderate aspect ratios has enhanced the attractiveness of stellarator reactors by combining the well-known advantages of torsatrons (current-free, steady-state operation and natural divertors) with the additional advantages of compact size and high-beta operation in the second stability regime. These compact torsatron reactors[2] are projected to have major radii $R_0 = 8$–11 m vs the $R_0 = 20$–25 m projected for other stellarator approaches.[3,4] However, the existence of a relatively large helical variation in the magnetic field strength, combined with toroidal effects at low aspect ratio, raises concerns about alpha-particle confinement in compact torsatron reactors. A relatively large fraction ($\sim 1/3$) of the particles are helically trapped in these devices. Radial electric fields can prevent the loss of helically trapped particles through $\mathbf{E} \times \mathbf{B}$ poloidal orbit rotation,[5,6] but only when a particle's kinetic energy W is on the order of or less than its potential energy in the electric field [$W \lesssim e\Phi$ where typically $e\Phi \sim (2$–$3)kT$]. Charged fusion products and energetic ions created by plasma heating systems have energies higher than those for which electric fields provide confinement, and the reduction of heating power associated with the loss of these energetic particles must be considered in designing torsatron reactors.

While extensive work has been done on alpha-particle losses in tokamak reactors,[7] relatively little work has been done for stellarators. Ho and Kulsrud[8] estimated indirect particle and energy losses due to scattering of alpha particles into a small perpendicular loss region. Other authors[9–11] developed analytic descriptions for the bounce-averaged guiding-center orbits of low- and moderate-energy trapped particles. However, these studies were concerned with understanding and classifying orbits, rather than with determining the fraction of energetic alpha particles lost, and they concentrated on higher-aspect-ratio magnetic configurations approximated by simple expressions for the magnetic field. The complicated magnetic field structure of low-aspect-ratio torsatrons and the large deviations of very energetic particle orbits from a magnetic surface, both of interest here, make an analytic treatment intractable.

The purpose of this paper is to investigate the loss of alpha particles and alpha-particle heating in compact torsatron reactors using realistic descriptions of the magnetic field strength and accurate methods for computing the guiding-center orbits. The base-case configurations studied are described in Sec. II, and the methods for computing the alpha-particle losses are summarized in Sec. III. Orbit losses

for the base-case configurations are given in Sec. IV. Numerical and approximate analytic solutions to the Fokker-Planck equation are used to estimate additional alpha-particle losses arising from pitch-angle scattering in Sec. V. Consequences for torsatron reactor design are discussed in Sec. VI. Sensitivity to the magnetic field structure is then addressed, and a figure of merit for assessing the particle confinement properties of a magnetic configuration is found in Sec. VII. In Sec. VIII, the confinement figure of merit is used to demonstrate how alpha-particle confinement in low-aspect-ratio torsatron reactors might be improved.

II. MAGNETIC CONFIGURATIONS STUDIED

Torsatrons produce toroidally nested, closed magnetic surfaces similar to those in tokamaks, but without a net driven current in the plasma. The necessary helical (toroidal plus poloidal) magnetic field is produced solely by unidirectional currents in external helical coils and hence is inherently steady state. Figure 1 shows the helical coils for the three base compact torsatron reactors studied here; these are the configurations of Ref. 2, with $M = 6$, 9, and 12 toroidal field periods. The $M = 12$ reactor is a scaled-up version of the Advanced Toroidal Facility (ATF) configuration,[12] and the $M = 6$ and $M = 9$ reactors are based on configurations obtained by poloidally modulating the helical field (HF) winding trajectory to retain the favorable magnetohydrodynamic (MHD) properties of ATF at lower aspect ratio. These configurations have moderate shear, small magnetic wells, and rotational transforms (ι) that range from about 1/3 on axis to about 1 at the plasma edge.[1] As the coil aspect ratio $A_c = R_0/a_c$ decreases, more space becomes available between the HF windings for access to blankets, shields, etc. Here a_c is the mean radius of the HF winding on the circular cross-section torus. The modulation of the HF winding is given by

$$\phi_s = \left[\theta_s - \sum_n \alpha_n \sin(n\theta_s)\right] \ell/M, \tag{1}$$

where ϕ_s and θ_s are the toroidal and poloidal angles in real space, the α_n are the modulation coefficients, and the poloidal symmetry number $\ell = 2$.

The principal configuration and device parameters for the reactor cases studied[2] are given in Table I. For all three cases, the magnetic field on the magnetic axis $B_0 = 5$ T, the volume-averaged density $\langle n \rangle = 2 \times 10^{20}$ m^{-3}, and the thermal fusion power $P_f = 4$ GW. These particular cases are attractive because of their relatively small size ($R_0 = 8.4$–11.1 m), moderate temperatures (central ion temperature

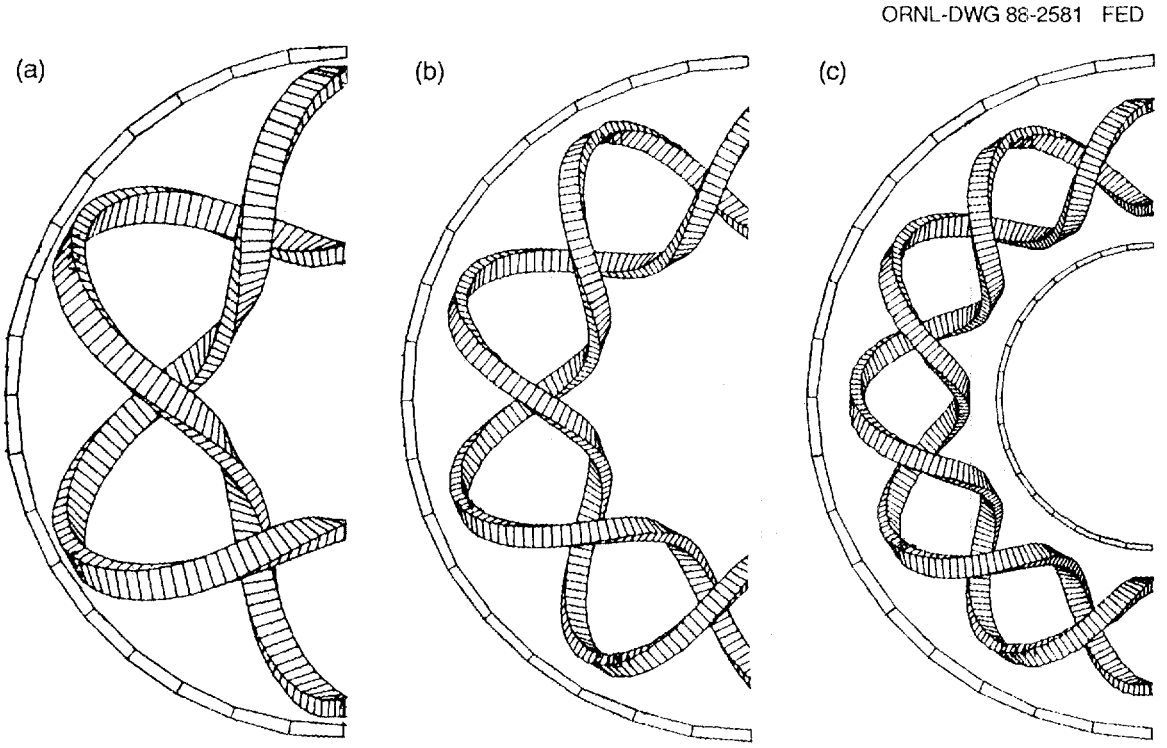

Fig. 1. Top views of coil geometry for (a) CT6, (b) CT9, and (c) CT12 base reactor cases.

TABLE I

Compact Torsatron Reactor Parameters

	Reactor case		
	CT6	CT9	CT12
Configuration Parameters			
Number of field periods, M	6	9	12
HF winding modulation			
α_1	0.446	0.275	0
α_2	−0.079	−0.0435	0
α_3	0.029	0	0
α_4	0.0009	0	0
Coil aspect ratio, R_0/a_c	2.50	3.24	4.49
Plasma aspect ratio, $R_0/\bar{a}$	3.87	4.66	7.78
Reactor Parameters			
Major radius, R_0 (m)	8.37	10.54	11.13
Plasma radius, $\bar{a}$ (m)	2.16	2.26	1.43
Central ion temperature, T_{i0} (keV)	11.9	10.4	14.4
Central electron temperature, T_{e0} (keV)	12.7	11.1	14.4
Volume-average beta, $\langle\beta\rangle$ (%)	7.2	6.3	9
Power to ignite, $P_{heating}$ (MW)	≃33	≃30	≃25
Neutron wall loading, Γ_n (MW/m^2)	3.38	2.69	3.92
Net electric power (MW), $\eta = 0.36$	1934	1897	1879
Mass utilization [kW(e)/tonne]	206	172	228

$T_{i0} = 10.4$–14.4 keV), efficient use of magnetic field ($\langle\beta\rangle = 6.3$–$9\%$), moderate neutron wall loading ($\Gamma_n = 2.7$–3.9 MW/m^2), moderate power to reach ignition (25–33 MW), and high mass utilization [170–230 kW(e)/tonne].

The simplest expression for the magnitude of the magnetic field of a toroidal stellarator is given by

$$B = B_0[1 - \epsilon_t \cos\theta + \epsilon_h(r)\cos(\ell\theta - M\phi)] \ , \tag{2}$$

where the cos θ term represents the finite toroidicity, as in a tokamak; $\epsilon_t = r/R_0 = (1/A)(r/\bar{a})$, where $\bar{a}$ is the average radius of the last closed magnetic surface and $A = R_0/\bar{a}$ is the plasma aspect ratio; and $\epsilon_h(r) \propto (r/\bar{a})^\ell$ is the normalized amplitude of the dominant helical ripple component of the stellarator field with poloidal symmetry number ℓ. While the approximation of Eq. (2) is useful for unmodulated HF winding laws ($\alpha_n = 0$) at large aspect ratio, the large poloidal modulation and the low toroidal aspect ratio for compact torsatrons produce a rich spectrum of HF harmonics. Therefore, we choose to represent the magnitude of the more realistic magnetic fields of interest here in the particular set of flux coordinates called Boozer coordinates,[13]

$$B = B_0 \sum_{n,m} B_{n,m}(\psi)\cos(n\phi - m\theta) \ , \tag{3}$$

where $2\pi\psi$ is the toroidal flux. The radial variable r is related to the toroidal flux through an approximation $\psi \simeq B_0 r^2/2$. The poloidal and toroidal angles (θ and ϕ) are chosen to make the field lines straight in this coordinate system (the rotational transform ι is constant on each flux surface). Equation (2) or (3) is sufficient to specify the magnetic field because only the magnitude of the field, and not its vector components, is required when the guiding-center orbit equations are written in Boozer coordinates [see Eq. (4)]. Each term in Eq. (3) is the magnitude of a divergence-free vector field, so the effect of individual terms can be studied without introducing nonphysical effects into the particle orbits. The same is true of the field magnitude given by Eq. (2) when θ and ϕ are the Boozer coordinates and $r \propto \sqrt{\psi}$, as we use it, but not when the usual space variables are used. The constraint of zero net current on each flux surface places restrictions on the form of $\epsilon_h(r)$ in Eq. (2) and $B_{n,m}(\psi)$ in Eq. (3), so arbitrary forms cannot be considered.

Figure 2 shows the largest $B_{n,m}$ values vs $\rho \equiv \sqrt{\psi/\psi(\bar{a})} \simeq r/\bar{a}$ for the $M = 6$ configuration. The largest term (not shown) is $B_{0,0}$, the average value of the magnetic field on a flux surface. $B_{0,0}$ is close to 1 for all values of ρ. $B_{0,-1}$ ($= -\epsilon_t$) is the $1/R$ variation of the field and varies as ρ. $B_{6,2}$ ($= \epsilon_h$) is the dominant helical

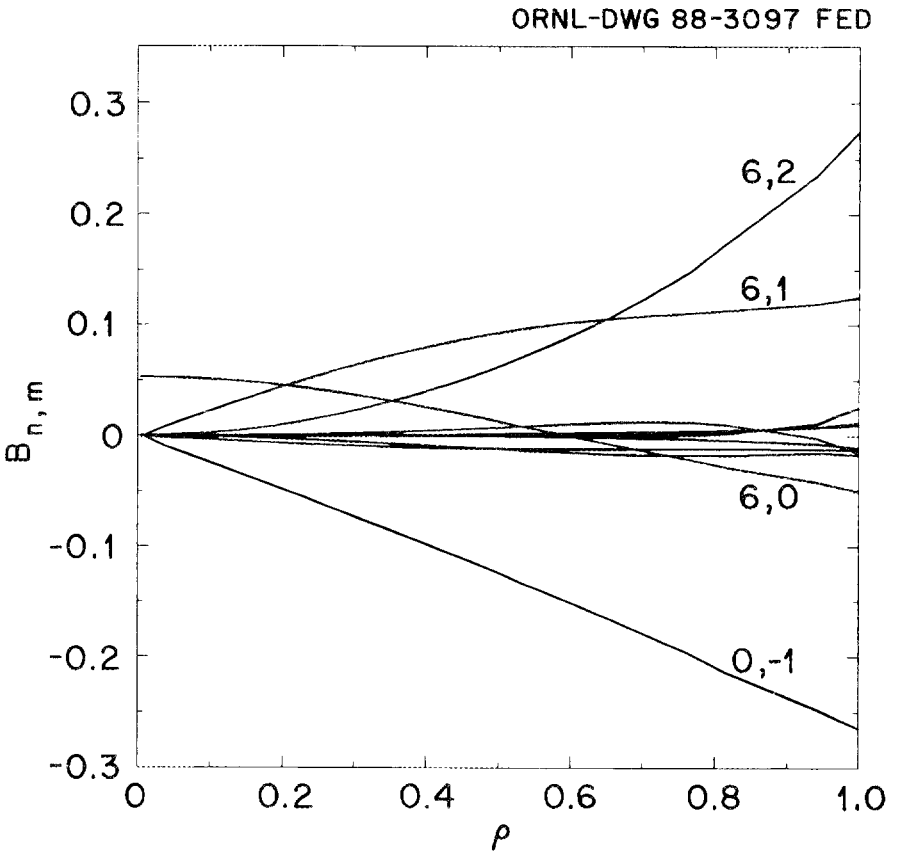

Fig. 2. Spatial variation of the magnetic field harmonics for the CT6 case.

harmonic and varies as ρ^2. The $B_{6,1}$ and $B_{6,0}$ terms, which result from the poloidal modulation of the HF winding trajectory and nonlinear mixing of the toroidal and helical effects, are also significant and cannot be neglected. The other terms are considerably smaller. We use 12 terms, with values down to $\lesssim 10^{-4}$, in this study. The relative magnitudes of the $B_{n,m}$ for the $M = 9$ and $M = 12$ cases are approximately the same as those for the $M = 6$ case but, along with $B_{0,-1}$, generally decrease with increasing M.

III. CALCULATION OF ALPHA-PARTICLE LOSSES

The loss of alpha-particle heating power has two components: a direct loss that occurs when alpha particles are born in the loss region and an indirect loss that results from the collisional diffusion of alpha particles into the loss region. These direct and indirect losses can be estimated independently when the loss region does not depend on energy. We use orbit-following techniques to map out the collisionless loss region; the indirect losses are estimated from solutions to the Fokker-Planck equation, as described in Sec. V. Electric-field effects are ignored because they are small for 3.5-MeV alpha particles.

The collisionless guiding-center drift equations in magnetic coordinates (ψ, θ_0, χ) are given by[13–15]

$$\begin{aligned}
\dot{\psi} &= -\frac{\partial \Phi}{\partial \theta_0} - \left(\frac{\mu}{e} + \frac{eB}{m}\rho_\parallel^2\right)\frac{\partial B}{\partial \theta_0} , \\
\dot{\theta}_0 &= \frac{\partial \Phi}{\partial \psi} + \left(\frac{\mu}{e} + \frac{eB}{m}\rho_\parallel^2\right)\frac{\partial B}{\partial \psi} , \\
\dot{\chi} &= \frac{eB^2}{m}\rho_\parallel , \\
\dot{\rho}_\parallel &= -\frac{\partial \Phi}{\partial \chi} - \left(\frac{\mu}{e} + \frac{eB}{m}\rho_\parallel^2\right)\frac{\partial B}{\partial \chi} ,
\end{aligned} \tag{4}$$

where θ_0 is a field line label, $\chi = \int B\, dl$, Φ is the electric potential, and the dot indicates a time derivative. The quantities m, q, W, μ, and $\rho_\parallel = (v_\parallel/v)\sqrt{2mW/qB}$ are, respectively, the particle's mass, charge, kinetic energy, magnetic moment, and parallel gyroradius. The quantities v and $v_\parallel$ are the magnitude of the velocity and the velocity component parallel to $\mathbf{B}$. The variables θ_0 and χ are related to the poloidal and toroidal angle variables[13] by

$$\begin{aligned}
\chi &= g(\psi)\phi + I(\psi)\theta , \\
\theta &= \theta_0 + \iota(\psi)\phi ,
\end{aligned} \tag{5}$$

where $g(\psi)$ is proportional to the poloidal current outside a flux surface and $I(\psi)$ is proportional to the toroidal current inside a flux surface.

By rewriting Eq. (4) in normalized variables, one can show that for a given configuration (B and Φ prescribed) the orbit equations depend only on two dimensionless parameters, the normalized gyroradius $\delta = \sqrt{2mW}/qB_0\bar{a}$ and the ratio of the particle's potential energy in the electric field to its kinetic energy $\gamma = q\Phi_0/W$. The device parameters enter only through δ, and the particle energy enters through δ and γ. For 3.5-MeV alpha particles, $\gamma \ll 1$ and is ignored here.

For these calculations, particles were started from a given flux surface with a random, uniform distribution in pitch, poloidal, and toroidal angles. Typically 128 to 256 particles, selected via a stratified sampling scheme, were used for each starting flux surface, but as many as 512 were used to verify that the estimates of the loss fractions had converged sufficiently. Stratified sampling, which involves dividing the sampling region into a number of subregions, is a particularly effective method for reducing the variance in the estimated collisionless loss, because it allows for heavier sampling near the boundary of the loss region. To produce a uniform distribution of starting weights on a flux surface, each particle was weighted by the Jacobian in magnetic coordinates ($1/B^2$). Each particle was followed until it (1) crossed the plasma boundary, taken to be near the $\iota = 1$ surface; (2) made two poloidal revolutions; or (3) exceeded a preset time cutoff, typically taken to be several hundred helical bounce periods.

IV. ORBIT LOSSES

Because of the three-dimensional nature of stellarator fields, a convenient way of displaying stellarator loss regions is difficult to find. Even with energy fixed, as it is here, four variables (three real space and one velocity) would be needed if the conventional representation were used. We choose a normalized magnetic moment μ^* and the minimum normalized radius along the orbit $\rho_{min} = \sqrt{\psi_{min}/\psi(\bar{a})}$ to identify individual orbits; Fig. 3 shows a scatter plot of lost and confined orbits for 3.5-MeV alpha particles in the base $M = 6$ reactor. Here μ^* is the magnetic moment μ normalized to a range between -1 and $+1$:

$$\mu^* \equiv \frac{v_\parallel}{|v_\parallel|}\frac{B_n(\bar{a})\mu}{W} ,$$

where $B_n(\bar{a})$ is the minimum magnetic field in the plasma, which occurs at the plasma edge ($\rho_{min} = 1$). The constant μ/W factor in μ^* can be written as

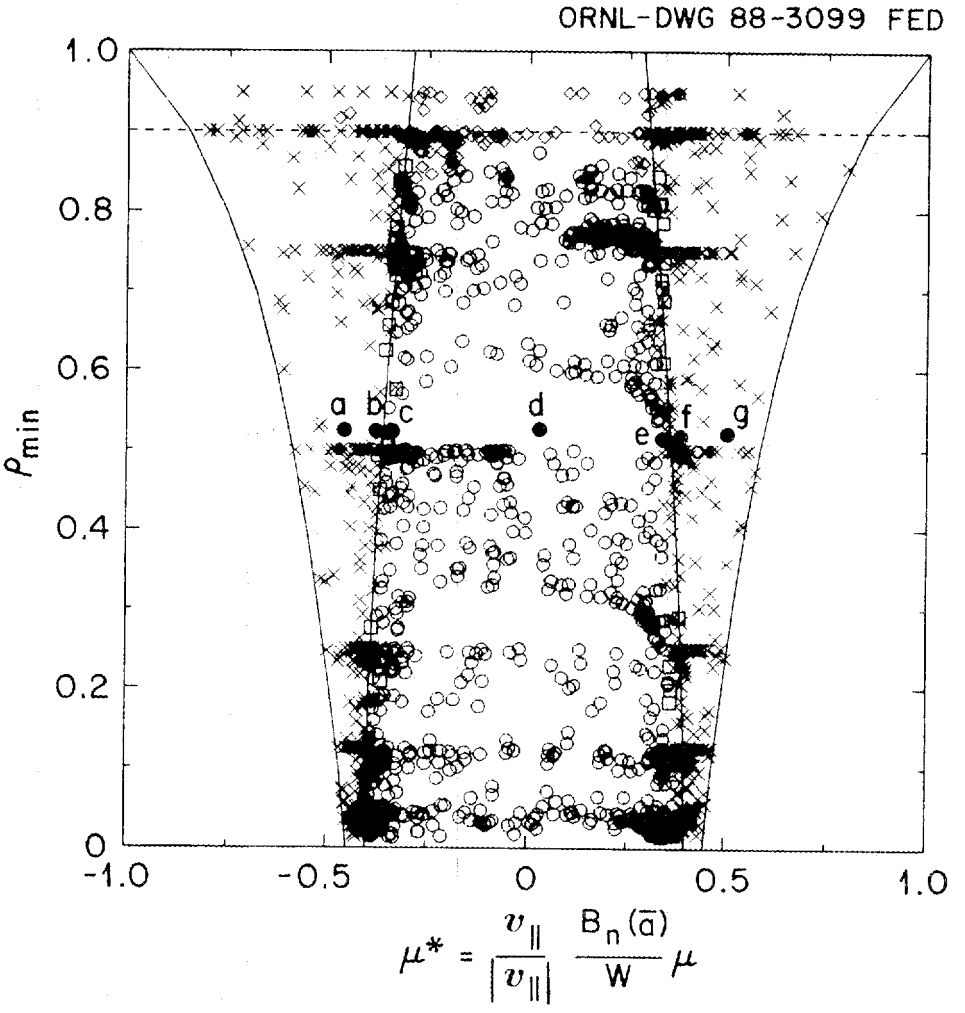

Fig. 3. Constants of motion for alpha-particle orbits in ρ_{min}-μ^* space for a CT6 reactor. The letters (a) through (g) refer to orbits in Fig. 4.

$(v_\perp/v)^2/B$ in general and as $1/B_{refl}$ for trapped particles, which reflect ($v_\parallel = 0$) at $B = B_{refl}$, the maximum value of field along the orbit. Here $v_\perp$ is the magnitude of the velocity component perpendicular to **B**. Passing particles have $(v_\perp/v)^2 < 1$ and $B < B_{refl}$. The boundary between trapped particles and passing particles is given by $|\mu^*| = B_n(\bar{a})/B_x$ and is indicated by the nearly vertical lines in Fig. 3. Here B_x is the maximum value of B for a given ρ_{min}.

The circles in Fig. 3 indicate confined passing-particle orbits, and the diamonds indicate lost passing-particle orbits. Lost trapped-particle orbits are shown as crosses, and confined trapped-particle orbits are shown as squares. The rightmost and leftmost curves are simply the boundaries for the space where $B = B_n$, the minimum value of B for a given ρ_{min}, and represent the loci of the most deeply trapped particles. The ratio $\mu^*(B_n)/\mu^*(B_x) = B_x/B_n$ gives the field ripple, which is nonzero on the axis ($\rho_{min} = 0$) and increases with ρ_{min} for the $M = 6$ configuration in Fig. 3. The points labeled (a) through (g) in Fig. 3 show the locations of some characteristic orbits in this space. Figure 4 shows these orbits, the variation of B along a typical field line, and the contours of constant B_{min} for this configuration. B_{min} is the minimum value of B along ϕ for a given θ and ψ, as opposed to B_n, which is the minimum value of B on a given flux surface. As discussed below, contours of constant B_{min} are useful approximations to the trapped-particle orbits.

When $|\mu^*| < B_n(\bar{a})/B_x$, the particles are passing [orbits (c) and (d)], and the details of the orbits are sensitive to the sign but not the magnitude of μ^*. The excursion that a passing particle makes from its ρ_{min} flux surface is composed of a deviation on the order of a poloidal gyroradius, resulting from the axisymmetric component of the magnetic field, and a higher-frequency oscillation in the field ripple. In these configurations, co-passing (μ^* and $v_\parallel > 0$) particle orbits are shifted inward in major radius, and counter-passing (μ^* and $v_\parallel < 0$) particle orbits are shifted outward. This shift causes a small asymmetry with respect to μ^* in the loss region, but, as can be seen by comparing the scatter plot in Fig. 3 with the low-energy trapped-passing boundary, the finite orbit excursion has only a small effect on the trapped-passing boundary. The main effect of the finite orbit excursion is to cause the loss of passing particles near the plasma edge. The horizontal dashed line in Fig. 3 indicates one poloidal gyroradius distance from the plasma edge. Particles that start in this region are likely to be lost, whether passing or trapped.

Essentially all trapped alpha particles are lost in the low-aspect-ratio $M = 6$ base configuration. Helically trapped particles move so as to conserve the helical bounce action $\oint v_\parallel dl$. For the most deeply trapped particles, this corresponds to

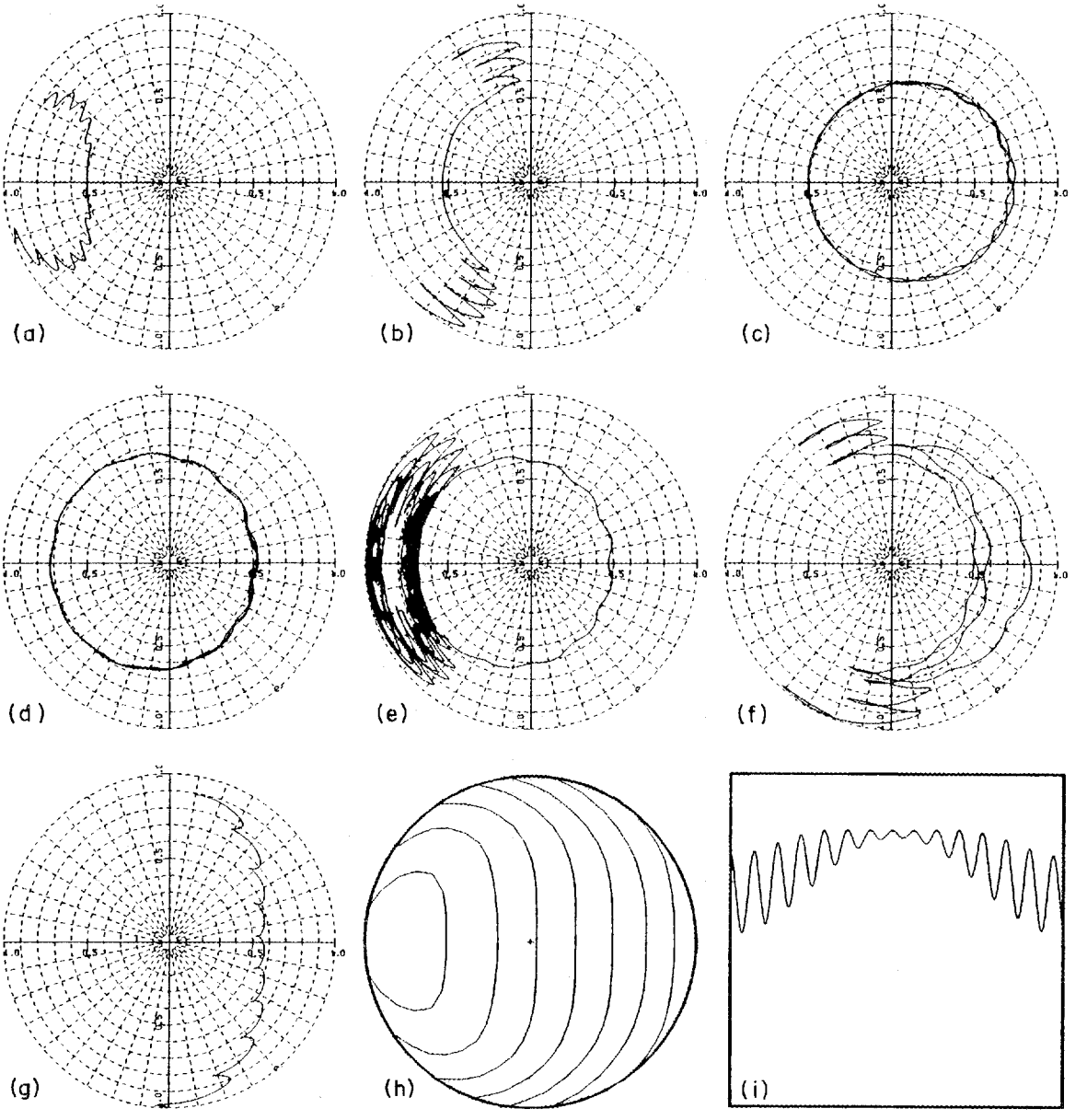

Fig. 4. (a) through (g): Characteristic orbits for the CT6 reactor. (h) Contours of constant B_{min}. (i) Variation of B along a field line.

motion along contours of constant B_{min}. Less deeply trapped particles also tend to drift along constant-B_{min} contours. If these B_{min} contours do not close in the plasma region, the helically trapped particles leave the plasma volume within a few bounces [orbits (a) and (g)]. Collisionless detrapping is common but is usually followed by retrapping, either directly [orbit (b)] or after several toroidal bounces [orbit (f)]. Alpha particles may drift a significant distance radially while in the toroidally trapped part of their orbits. This radial drift is similar to the stochastic diffusion[16] found in tokamaks with toroidal field coil ripple. A small population of transitional particles is confined [orbit (e)]. These transitional particles repeatedly detrap and retrap in the shallow helical wells on the inboard side of the torus in a manner that is symmetric about the horizontal midplane so that the net radial drift is zero. These particles occupy a boundary region between the trapped and confined regions (squares in Fig. 3) and constitute only a small fraction of the trapped-particle population.

The fraction of confined alpha particles is shown in Fig. 5 as a function of normalized starting radius ρ for the $M = 6$, 9, and 12 minimum-radius reactors. The losses are greater for the lower-aspect-ratio $M = 6$ and 9 configurations because the fraction of trapped particles is larger (18% for $M = 12$ and 30% for $M = 6$, with $\rho = 0.25$) and the confinement of these particles is poorer. The $M = 6$ configuration loses 96% of the trapped alpha particles, while the $M = 12$ case loses only 40%. This point is illustrated in Fig. 6, which compares the flux-surface-averaged fraction of confined alpha particles as a function of the pitch-angle parameter $\xi = v_{\|}/v$ for the $M = 6$ and $M = 12$ reactors. The small asymmetry with respect to the pitch-angle parameter for the $M = 6$ reactor results from the shift of the trapped-passing boundary discussed above. It appears that the more dramatic asymmetry for the $M = 12$ configuration also results from this shift and from the fact that deeply trapped particles are better confined than particles that are marginally trapped.

The loss region is very insensitive to the alpha-particle energy. Figure 7 shows the flux-surface and pitch-angle average of the fraction of alpha particles confined in the $M = 6$ base reactor for various values of the normalized gyroradius δ. These values of δ span a large range in particle energy, from $\simeq$15-keV D-T particles in the 8-m, 5-T reactor ($\delta = 8 \times 10^{-3}$) to 3.5-MeV alpha particles in a 4-m, 5-T ignition experiment ($\delta = 5 \times 10^{-2}$). Equivalently, $1/\delta = N$, the number of gyroradii across the plasma, which varies from 20 to 125 in Fig. 7. The solid curve is the fraction of passing particles at zero energy. Essentially all of the trapped alpha particles are lost from the $M = 6$ base configuration, even for small values of δ. The fraction

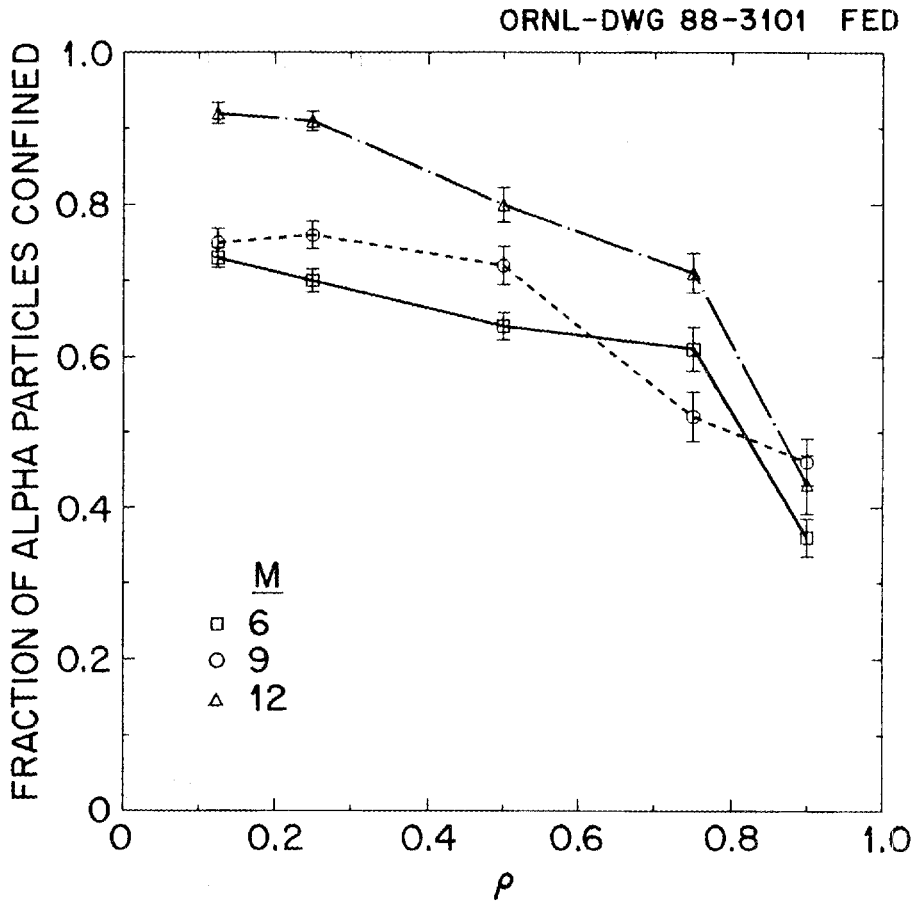

Fig. 5. Fraction of contained alpha particles for the CT6, CT9, and CT12 base reactor cases vs ρ.

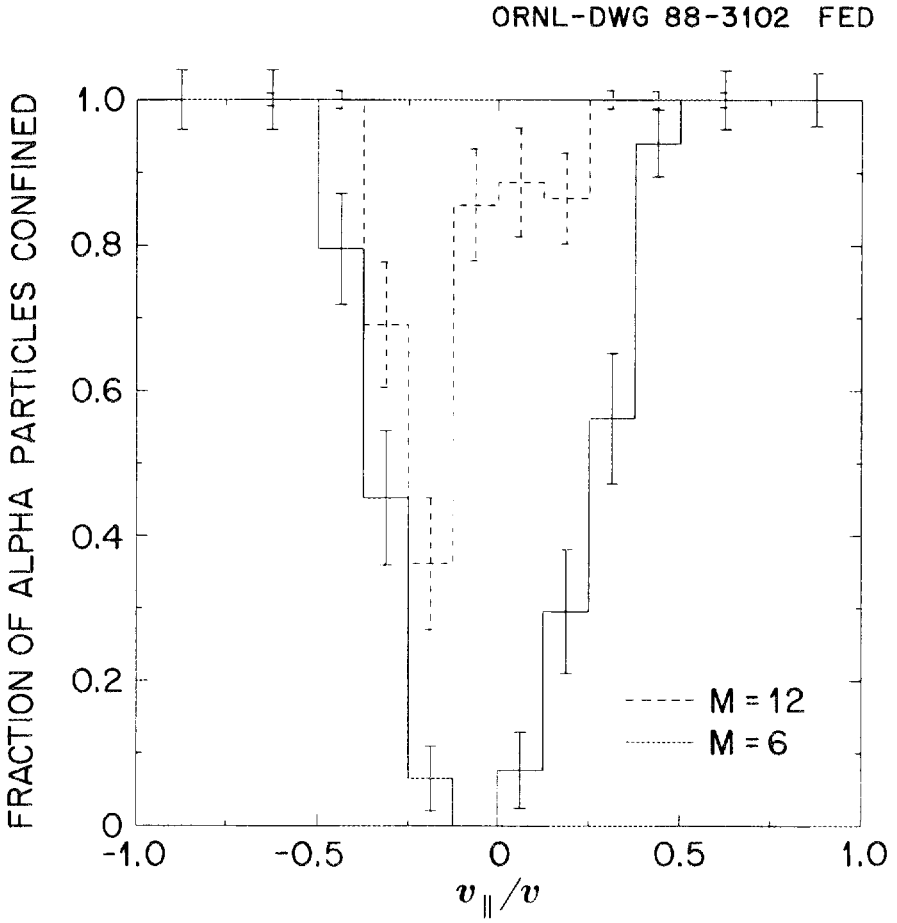

Fig. 6. Perpendicular loss region for the CT6 and CT12 configurations.

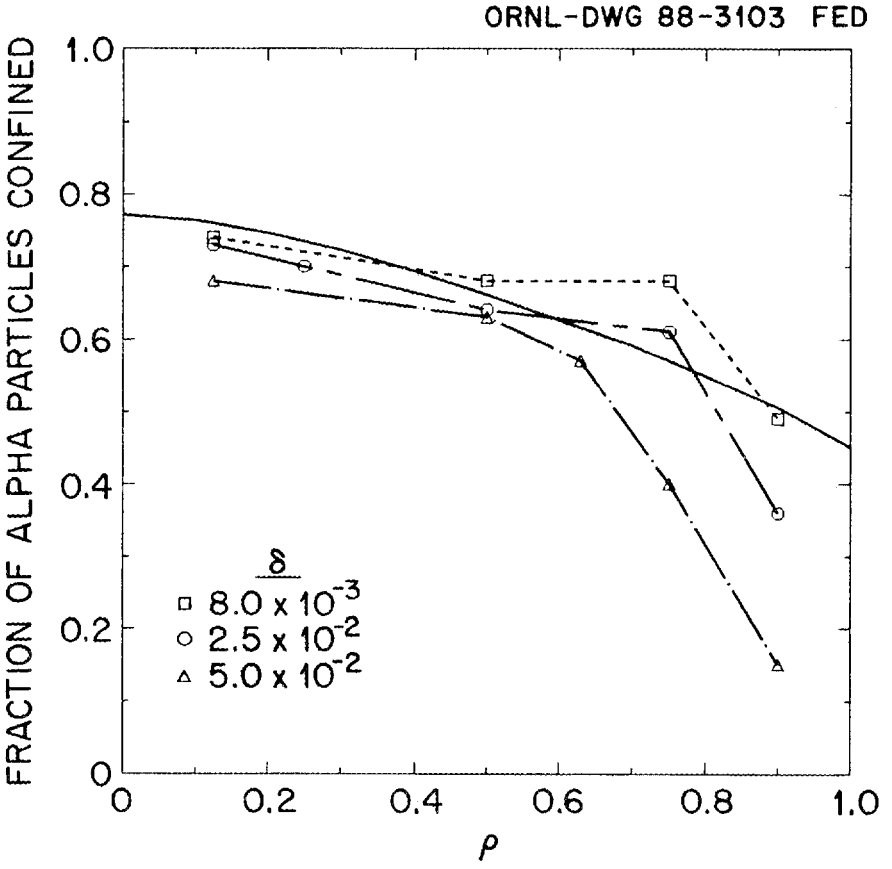

Fig. 7. Fraction of contained alpha particles for different values of δ in a CT6 reactor.

The fraction of alpha particles and power lost between 3.5 MeV and energy W is given as a function of W in Fig. 8, for $\xi_c = 0$ and $\xi_c = 0.3$, where ξ_c is the value of $|v_\parallel/v|$ at the edge of the loss region. Both the indirect and the direct losses (the value at $W = 3.5$ MeV) are included in Fig. 8, where $Z_{eff} = 1.5$ due to oxygen is assumed. The solid (dashed) lines are numerical results for alpha-heating (alpha-particle) losses, and the chain-dotted lines are the approximate solution for alpha-particle losses described in the Appendix. For comparison, the exact solution for particle losses for $\xi_c = 0$, taken from Ho and Kulsrud,[8] is also shown (chain-dashed curve). The agreement between the exact analytic solution, the approximate analytic solution, and the numerical results is excellent except very near 3.5 MeV, where the exact analytic solution experiences convergence problems. (The exact analytic solution and the numerical results overlie each other and are indistinguishable on this scale.)

Following an initial transient, which results from the steep gradients in the distribution function at $\xi = \xi_c$ near $W = 3.5$ MeV, the fraction of alpha energy lost rises nearly linearly with decreasing energy to ~15% at 100 keV. The particle loss fraction rises slowly to about W_{crit}, and then steeply because of the increased scattering cross section. The indirect component of the loss is nearly independent of the width of the loss region: 15% of the alpha-particle heating is lost because of scattering when $\xi_c = 0$, vs 13% when $\xi_c = 0.3$. When the loss region is of finite size, the number of particles available for scattering into the loss region is reduced by $(1 - \xi_c)$, but the average pitch angle through which a particle must scatter to reach the loss region is decreased by a corresponding amount. The finite loss region has a small effect on the particle loss fraction at low energy: 58% of alpha particles are lost above 100 keV because of scattering when $\xi_c = 0$, and 50% are lost when $\xi_c = 0.3$. The perpendicular loss region is thus effective at removing the alpha-particle ash, but at some penalty ($\simeq$15%) in the alpha-particle heating.

VI. IMPLICATIONS FOR TORSATRON REACTOR DESIGN

The fraction of alpha heating power lost from the $M = 6$, 9, and 12 base reactors is summarized in Table II for source profiles of the form $[1 - \psi/\psi(\bar{a})]^n$. These losses include both the direct collisionless losses and the estimate of scattering into the loss region. Because $\psi \propto r^2$, the $[1 - \psi/\psi(\bar{a})]^4$ form corresponds to parabolic density and temperature profiles. The results are relatively insensitive to the exponent of $1 - \psi/\psi(\bar{a})$ because of the slow variation of f_c with $\rho = \sqrt{\psi/\psi(\bar{a})}$, shown in Fig. 5.

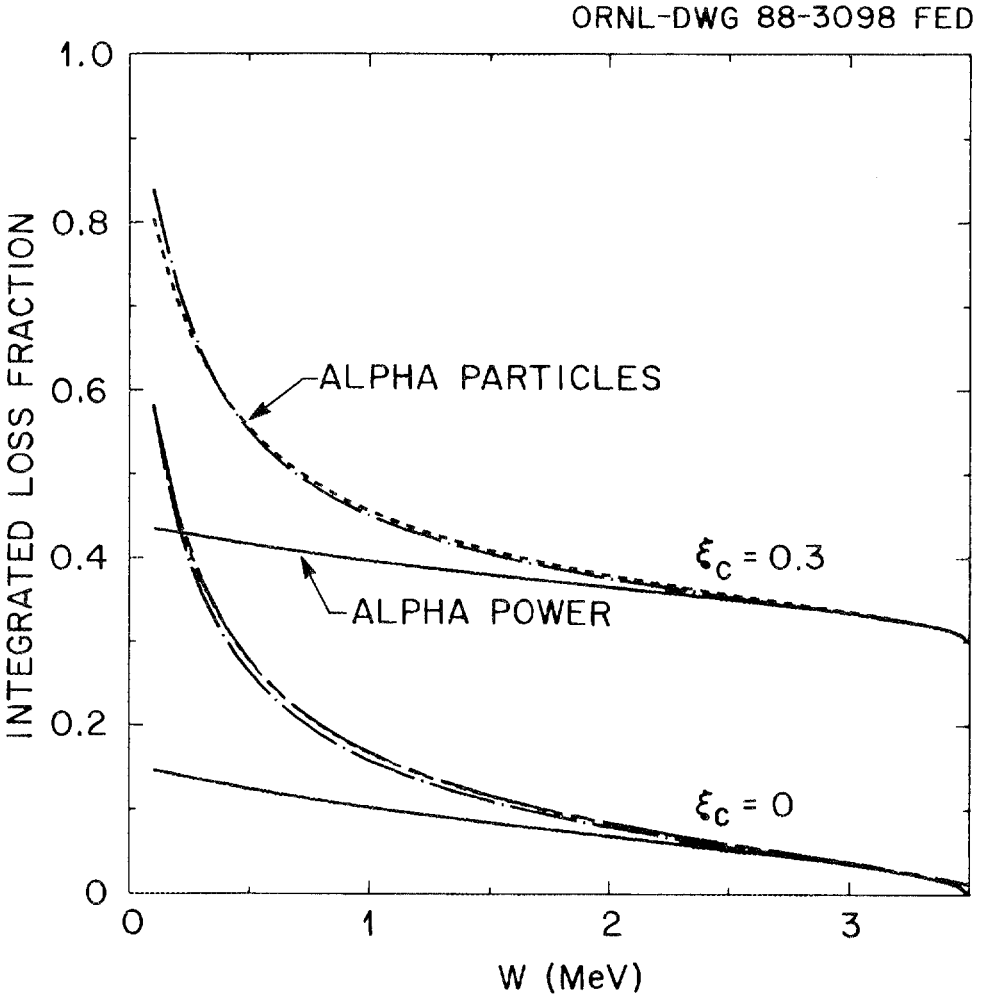

Fig. 8. Integrated fraction of particles and energy lost for alpha particles slowing down and scattering into loss regions at $v_{\|}/v = 0$ and $|v_{\|}/v| \leq 0.3$.

TABLE II

Fraction of the Alpha Power Lost for $M = 6$, 9, and 12 Base Reactors for Different Source Peaking Factors n Where the Source is $S_0 [1 - \psi/\psi(\bar{a})]^n$

	Alpha Power Lost (%)		
n	CT6	CT9	CT12
2	51 ± 1	48 ± 2	37 ± 1
4	46 ± 1	43 ± 2	32 ± 2
8	44 ± 1	41 ± 3	29 ± 2

The main impact of these losses is to increase the amount of heating power required for ignition. Table I indicates that heating to ignition requires $\simeq$33 MW for the $M = 6$ and $\simeq$25 MW for the $M = 12$ configurations without any alpha-particle losses. Calculations[2] with the WHIST transport code[20] show that these cases are thermally unstable for $Q = P_\alpha/P_{heating} > 5$–10, so the necessary heating power increases to 43–47 MW for $M = 6$ and 30–32 MW for $M = 12$. After the plasma ignites, the alpha-particle loss has only a beneficial effect: it aids in burn control by limiting the power available for the thermal excursion and channels the alpha-particle energy directly to the outside so that it does not end up on the vacuum vessel walls in degraded form with a higher sputtering rate.

Fortunately, the lost alpha particles exit the plasma in a very narrow helical strip between the HF windings,[6] so it should be possible to recover this energy externally. However, the space required for collecting this high-power-density flux will reduce that available for tritium breeding and increase the required neutron multiplication factor in the blanket (higher beryllium fraction). The loss region also serves as a helium-ash removal mechanism. Although alpha particles with energies below W_{crit} are lost, the background D-T plasma ions are unaffected up to energies of $\sim(2$–$3)T$. The same general results will also hold for D-T ignition experiments. These devices[2] have the same B_0 as the reactor cases but are smaller in size ($R_0 \simeq 4$ m). The short-dashed curve in Fig. 7 shows the fraction of alpha particles confined in an $M = 6$ D-T ignition device.

Because the device parameters enter into the orbit equations only through the normalized poloidal gyroradius δ, we can extrapolate our results to applications other than reactors. The 3.5-MeV alpha particles in a reactor with $R_0 = 8$ m and $B_0 = 5$ T are equivalent to 140-keV protons in a next-generation experiment with $R_0 = 2$ m and $B_0 = 4$ T. The poloidal gyroradius is $\simeq$0.05 m in such a next-generation experiment, so high-energy ions with $r/\bar{a} \gtrsim 0.9$ would be lost. The near-perpendicular nature of the loss region and the relative insensitivity to energy indicate the need for plasma heating that does not produce a large population of energetic particles with small $|v_\parallel/v|$. Possible heating methods include electron cyclotron heating, tangential neutral beam injection, fundamental ion cyclotron heating, or ion Bernstein wave heating. Pitch-angle scattering is also more important in an experiment (in which the ratio W_{fast}/W_{crit} is much lower) than in a reactor, because, even though W_{crit} is lower ($9.3T_e$ for $H^0 \rightarrow D^+$, $14.8T_e$ for $H^0 \rightarrow H^+$, and $18.6T_e$ for $D^0 \rightarrow D^+$, vs $32T_e$ for $\alpha \rightarrow$ D-T), W_{fast} is much lower ($\lesssim$0.1 MeV vs 3.5 MeV).

VII. DEPENDENCE OF DIRECT ALPHA-PARTICLE LOSSES ON CONFIGURATION PROPERTIES

The direct alpha-particle loss determined in Sec. IV (up to ~1/3 of the total population in some cases) is large by tokamak standards; it is worthwhile to try to reduce it both because of the direct loss of alpha-particle heating and because of the increased heat transport from the thermal population that results from poorer confinement of trapped particles. Both effects increase the auxiliary heating power required for ignition. We focus on understanding the direct loss of alpha particles; the additional energy loss due to pitch-angle scattering is approximately independent of the direct loss but goes to zero if the direct loss is zero.

To understand how the direct loss of helically trapped alpha particles in low- to moderate-aspect-ratio torsatrons is influenced by the magnetic field structure, we have investigated the orbit confinement characteristics of a number of additional configurations. These variants of the base configurations were selected to provide a data base of widely varying configurations. They differ from the base configurations in that they have different currents in the vertical field (VF) coils, different modulations of the HF coils, or $\ell = 1$ HF windings in addition to the primary $\ell = 2$ HF windings. The orbit losses for the base and variant configurations are summarized in Table III. For convenience, we use the notation of Ref. 1: CT6 for the $M = 6$ compact torsatron configuration, CT9 for the $M = 9$ configuration, etc. (These configurations are called ATR-1, ATR-2, and ATR-3 in Ref. 2.) For the base configurations, the plasma radius is fixed at 2 m, rather than at the minimum achievable reactor radius, for clearer comparisons. The CT12− (CT12+) configuration is the CT12 base configuration shifted in (out) by changes in the dipole component of the vertical field, while for CT12I the quadrupole component of the vertical field in CT12 is changed to increase the rotational transform on axis, $\iota(0)$. The CT9U and CT9α1 configurations have simplified winding trajectories; CT9U has an unmodulated winding trajectory, while CT9α1 retains only one modulation coefficient [α_1 in Eq. (1)]. The CT9L1A and CT9L1B configurations are created by adding an $\ell = 1$ HF winding to the CT9 configuration.

The results in Table III show no clear correlation between trapped-particle confinement and aspect ratio. For example, the fraction of trapped particles lost from the moderate-aspect-ratio CT12 configurations varies from 0 to 100%, depending on how the VF coils are used to alter the magnetic configuration. For a starting radius $\rho = 0.5$, the CT9L1B configuration with aspect ratio $A = 6.2$ loses fewer

TABLE III

Orbit Losses for Base and Variant Configurations

Configuration	Aspect ratio A	Starting radius ρ_0	Particles lost (%)		Case number
			Total	Trapped	
CT6	3.9	0.125	27	100	1
		0.5	36	97	2
		0.75	39	94	3
CT7	3.3	0.125	24	80	4
		0.5	30	82	5
CT9	4.7	0.125	25	95	6
		0.5	28	86	7
		0.75	42	89	8
CT12	7.8	0.125	9	47	9
		0.5	25	79	10
		0.75	34	82	11
CT6–	4.2	0.125	26	98	12
CT9L1A	8.0	0.125	7	36	13
		0.5	14	49	14
CT9L1B	6.2	0.125	13	50	15
		0.5	20	64	16
		0.75	37	88	17
CT9U	5.1	0.25	27	98	18
CT9α1	5.2	0.25	30	100	19
CT12–	7.6	0.125	0	0	20
		0.5	10	33	21
		0.75	26	64	22
CT12+	8.4	0.125	22	100	23
CT12I	7.8	0.125	0	0	24
		0.5	11	38	25

trapped particles than the higher-aspect-ratio ($A = 7.8$) CT12 (64% vs 79%), and the lowest-aspect-ratio device addressed, CT7 with $A = 3.3$, loses a smaller fraction of trapped particles than CT12+ with $A = 8.4$ (80% vs 100%). Better understanding of the configuration properties that determine the loss of helically trapped alpha particles is clearly needed.

A useful measure of the orbit confinement properties of a magnetic configuration can be deduced by examining the orbits and contours of B_{min} for a simple magnetic configuration and then applied to the more complicated cases in Table III. For this model, we choose the field expression of Eq. (2) with $B_0 = 5$ T; $\epsilon_t = \epsilon_t^a r/\bar{a}$, so that $\epsilon_t^a = 1/A$; $\epsilon_h = \epsilon_h^a (r/\bar{a})^2$, so that $\ell = 2$; and $M = 6$. A starting radius $\rho = 0.25$, $A = 5$, $\bar{a} = 2$ m, and $\iota(\rho) = 1/3 + 2/3\rho^2$ are used in the orbit calculations. Figure 9 shows poloidal projections of constant-B_{min} contours with deeply trapped orbits superimposed for four values of the parameter $p_2 = \epsilon_t^a/\epsilon_h^a = -B_{M,2}(\rho = 1)/B_{0,-1}(\rho = 1)$. When $p_2 \simeq 1$, only a small fraction of the constant-B_{min} contours are closed in the plasma region, and trapped particles are lost. As p_2 increases, more of the constant-B_{min} contours close in the plasma region, and the losses are reduced. For $p_2 \ll 1$, the particle losses are not correlated with closing of the constant-B_{min} contours, since particles are trapped primarily by the $1/R$ variation in B and the dominant loss mechanism is stochastic diffusion of the toroidally trapped orbits.

The confinement of trapped alpha particles in more complicated stellarator configurations is also correlated with the closing of the constant-B_{min} contours. This is demonstrated in Fig. 10, which shows the fraction of trapped particles confined as a function of $f_>$. The numbered points in Fig. 10 refer to the case numbers assigned to the configurations of Table III, and the triangles represent the model configurations with $A = 5$ or 10 and a range of p_2 values. The configurations represented in Fig. 10 have aspect ratios ranging from 3.3 to 10 and relative helical ripples (ϵ_h^a) ranging from 0.1 to 0.5. Here $f_>$ is a measure of the fraction of the constant-B_{min} contours that close in the plasma region, calculated as follows. If the constant-B_{min} contours are projected into the ρ-θ plane, as in Fig. 9, then $f_>$ is the ratio of the area $A_>$ inside the last closed B_{min} contour and outside the starting flux surface to the area in the annulus between the starting flux surface and the last closed flux surface. The area $A_>$ is shown schematically in Fig. 11. The fraction f_c of trapped particles that are confined can be fitted by the expression

$$\begin{aligned} f_c &= 1.61 f_>^2 , \qquad f_> < 0.79 , \\ f_c &= 1 , \qquad\qquad f_> > 0.79 , \end{aligned} \tag{6}$$

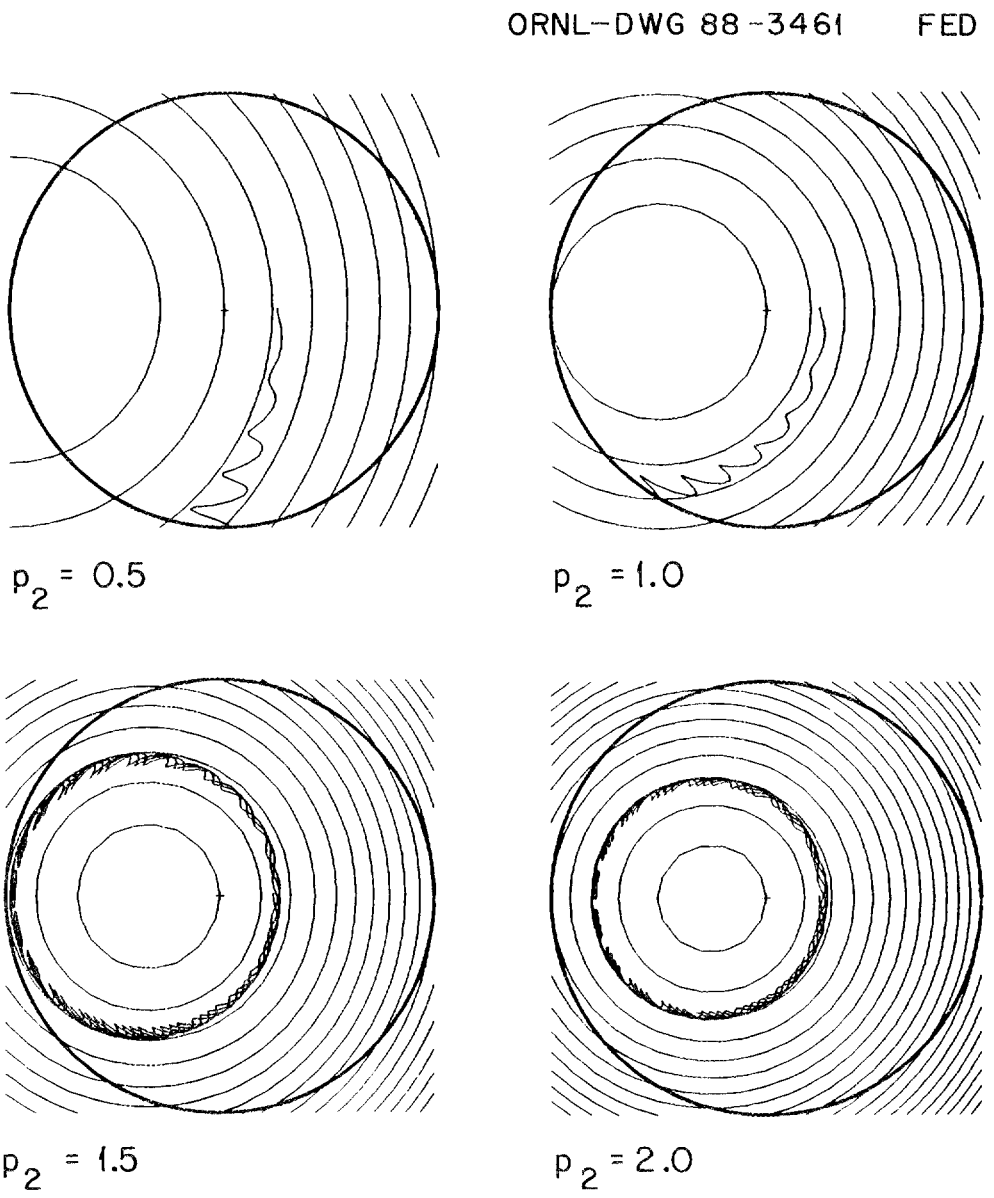

Fig. 9. Effect of varying p_2 on alpha-particle orbits. The constant-B_{min} contours are also shown.

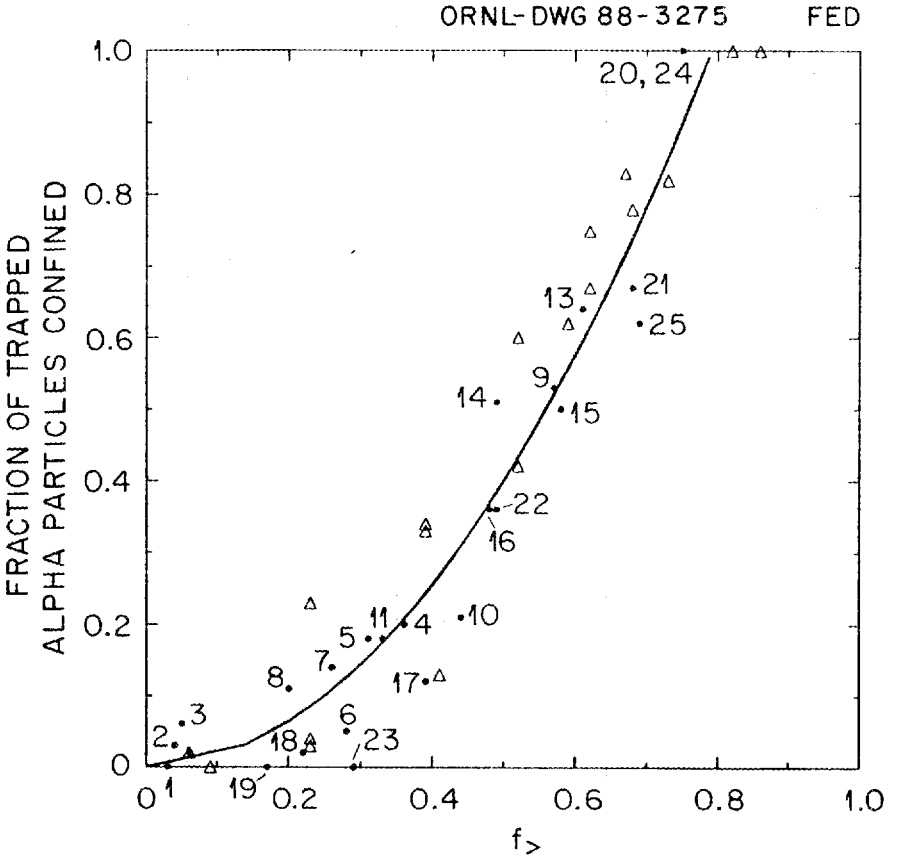

Fig. 10. Fraction of alpha particles that are confined vs $f_>$.

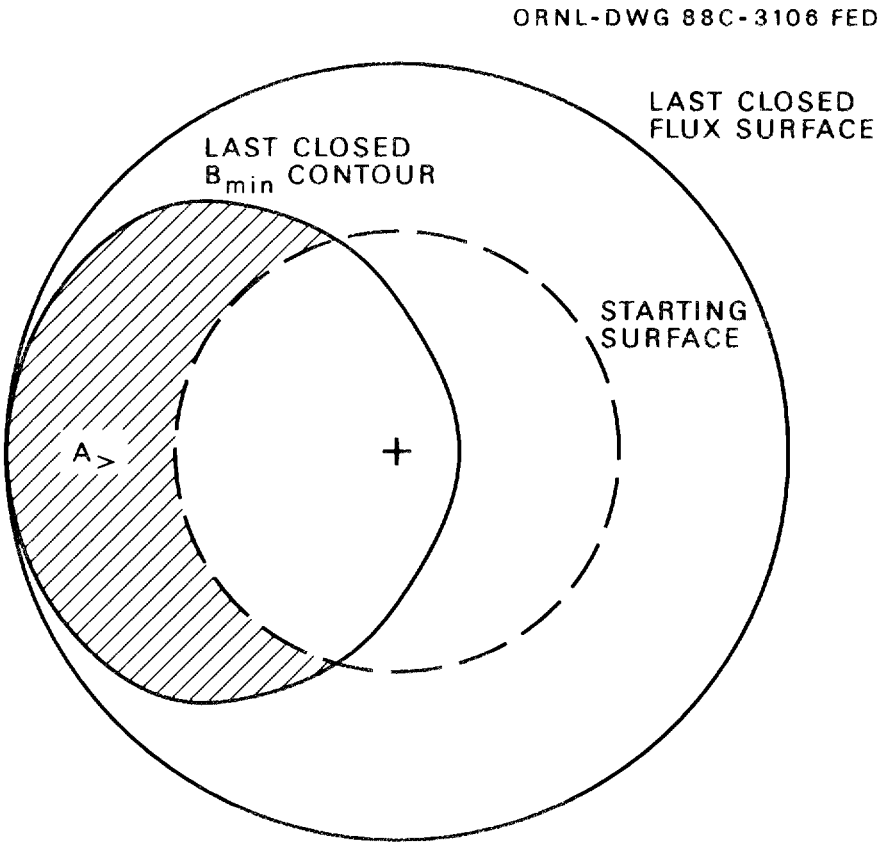

Fig. 11. Definition of the area $A_>$.

with an rms error of 0.08 (absolute). This expression holds for $\delta \simeq 0.02$, which corresponds to the case of 3.5-MeV alpha particles, $\bar{a} = 2$ m, and $B_0 = 5$ T. Similar expressions will hold for other values of the normalized gyroradius.

It is possible to find configurations with fractions of confined trapped alpha particles that deviate more from the curve [Eq. (6)] in Fig. 10 than the points shown. However, these configurations have either much greater shear (and larger losses) or much less shear (and smaller losses) than the ATF-like compact torsatron configurations studied here. Thus, we can use Eq. (6) as a fast means of evaluating the alpha-particle confinement properties of magnetic configurations with ATF-like rotational transform profiles, even configurations that otherwise differ considerably from the base compact torsatron configurations.

VIII. REDUCTION OF DIRECT ALPHA-PARTICLE LOSSES

To understand how direct alpha-particle losses might be reduced, we start with the model field given by Eq. (2) in order to isolate the role played by the lowest-order terms (ϵ_t and ϵ_h) in determining the alpha-particle losses. Additional helical ripple terms are then added to demonstrate how more complex field structures can improve alpha-particle confinement.

For the set of parameters used in discussing Fig. 9 [$M = 6$, $\ell = 2$, $B_0 = 5$ T, $\bar{a} = 2$ m, $\rho = 0.25$, and $\epsilon(\rho) = 1/3 + 2/3\rho^2$], but with $A = 5$ and 10, the fraction of helically trapped alpha particles lost is shown in Fig. 12. For a given value of p_2, the probability that a trapped alpha particle will be lost is relatively independent of aspect ratio, but the total losses decrease with A because of the decreasing fraction of helically trapped particles. When $p_2 \simeq 1$, symmetry-breaking effects are at their strongest, and essentially all trapped particles ($\simeq$95%) are lost. When $p_2 \ll 1$, particles are trapped primarily by the $1/R$ variation of B, the field is nearly axisymmetric, and the losses are small. Similarly, when $p_2 \gg 1$, the configuration is nearly helically symmetric, and helically trapped orbits are well confined. This is similar to the findings of Wakatani et al.,[9] who showed that trapped particle orbits close in the plasma region for large-aspect-ratio configurations when $p_2 \gg 1$ but not when $p_2 \sim 1$. Unfortunately, for the cases of most interest at low aspect ratio, ϵ_t^a is large ($\sim$0.2) and comparable to the dominant helical ripple term $\epsilon_h^a = B_{M,2}$, so $p_2 \sim 1$.

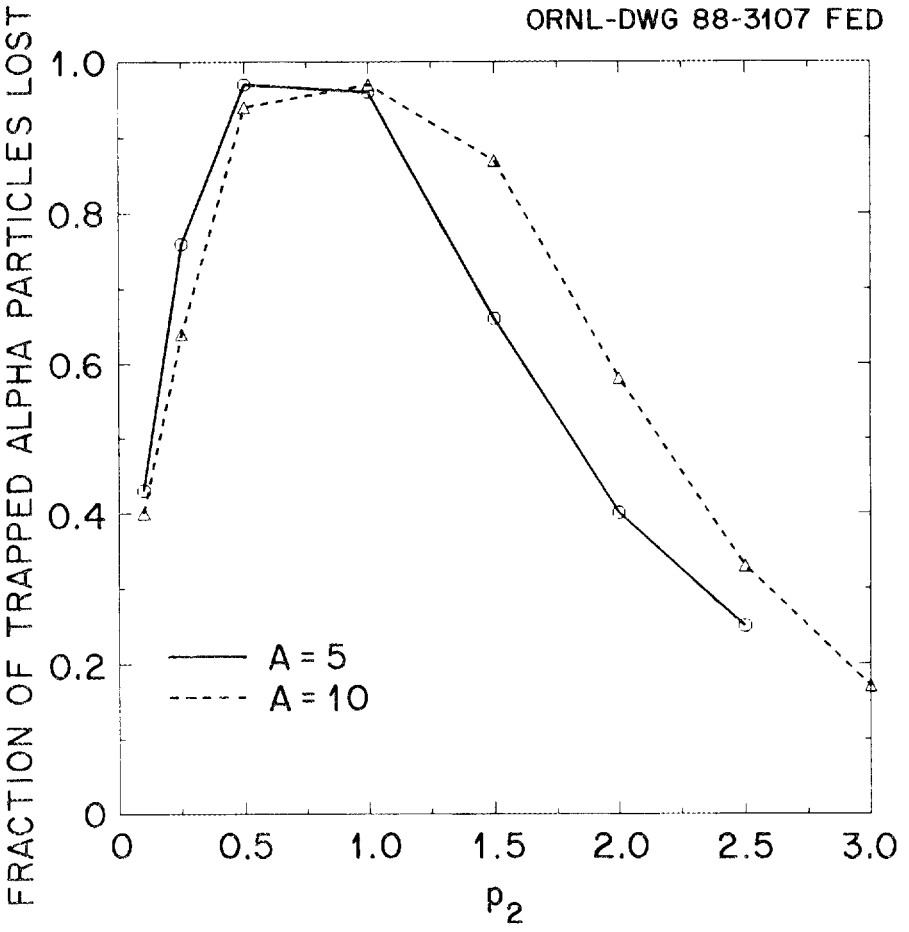

Fig. 12. Fraction of helically trapped alpha particles lost versus p_2.

However, it is possible to compensate for this situation with additional terms in B. Mynick et al.[21] have studied a σ-optimized field given by

$$B = B_0[1 - \epsilon_t \cos\theta + \epsilon_h(1 - \sigma\cos\theta)\cos(\ell\theta - M\phi)] \ , \tag{7}$$

which is the same as Eq. (2) with ϵ_h replaced by $\epsilon_h(1 - \sigma\cos\theta)$. Mynick et al. take $p_2 = 1$ and find minimum transport for $\sigma \simeq 1$. Using Eq. (6) for the relation between losses and $f_>$, we have estimated the fraction of alpha particles lost for this configuration with $A = 5$, $B_0 = 5$ T, $\bar{a} = 2$ m, and $\rho = 0.25$. The results are shown in Fig. 13. A band of zero losses approximately follows the curve $\sigma = 1/p_2$ from $\sigma = 1.4$, $p_2 = 0.73$, to $\sigma = 0.5$, $p_2 = 2$ (and beyond). By assuming that the constant-B_{min} contours are circles in the ρ-θ plane, one can show that constant-B_{min} contours, and consequently trapped-particle orbits, coincide approximately with flux surfaces when $\sigma = 1/p_2$. This should lead to reduced transport as well as improved alpha-particle confinement.

The added term in Eq. (7) increases the effective amplitude of ϵ_h on the inside major radius (or increases the field line length where it is reduced by the $1/R$ effect) and reduces ϵ_h on the outside major radius (or reduces the field line length where it is increased by the $1/R$ effect). The net effect is to make the field look more helically symmetric to trapped particles and hence have an effectively larger aspect ratio, similar to the M-S configuration.[22] It may be possible to achieve some of this effect by a different poloidal modulation of the HF winding trajectory.

Another, perhaps more straightforward, way to accomplish this might be by adding an $\ell = 1$ component to the field, perhaps with the proper $\ell = 1$ winding. The results of this calculation, for the same parameters used in Figs. 12 and 13, are shown in Fig. 14. We define $p_\ell = -B_{M,\ell}(\rho = 1)/B_{0,-1}(\rho = 1)$ for $\ell = 1$ and $\ell = 3$, similar to the definition p_2 used in Sec. IV for $\ell = 2$. Two bands of zero losses are shown: one triangular region at the bottom and another triangular wedge at $p_1 \simeq -1$ with $p_2 \gtrsim 1.3$. The variation of losses with p_2 shown in Fig. 12 is the line $p_1 = 0$ in Fig. 14. Better results are obtained if $p_1 \simeq -1$.

The additional term $-\sigma\cos\theta\cos(\ell\theta - M\phi)$ in Eq. (7) can be rewritten as $-\sigma/2\{\cos[(\ell+1)\theta - M\phi] + \cos[(\ell-1)\theta - M\phi]\}$, which introduces equal $\ell = 1$ and $\ell = 3$ terms in the field expansion with sign opposite to that of the $\ell = 2$ term. The effect of the added $\ell = 1$ and $\ell = 3$ terms is shown in Fig. 15 for $p_2 = 1$; the other field parameters are the same as those in Figs. 13 and 14. Similar to the transport calculation of Mynick et al.,[21] the losses are zero for $p_1 = p_3 \simeq -1/2$. However, other combinations of p_1 and p_3 also yield zero losses. The band of zero

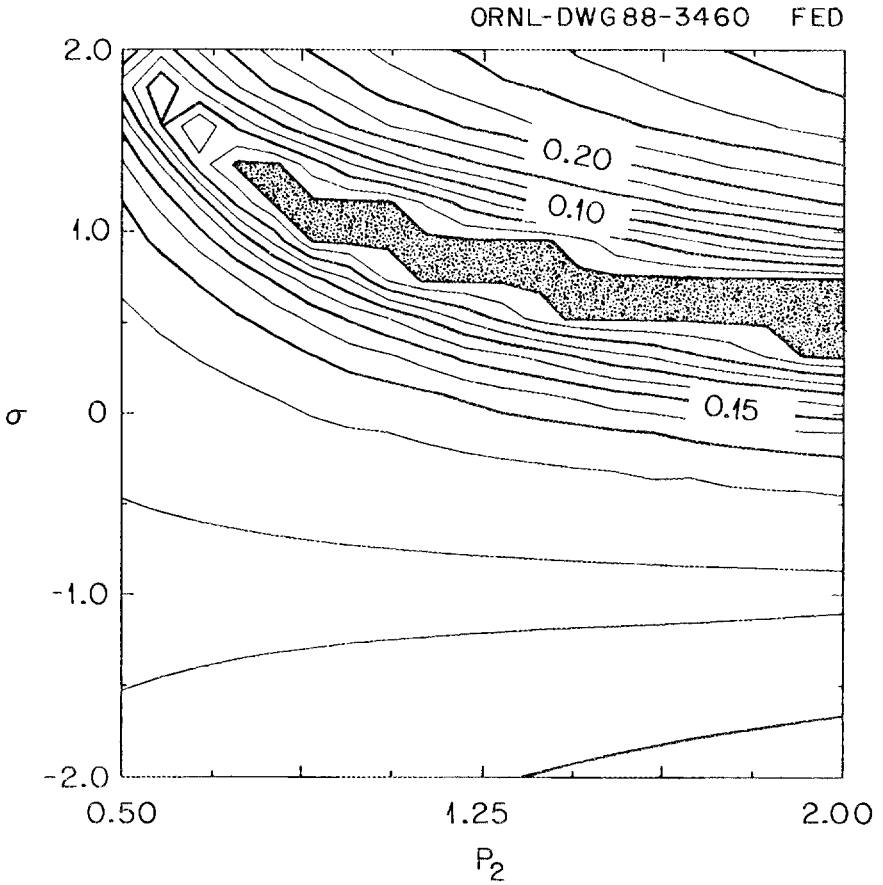

Fig. 13. Contours of constant alpha-particle losses in the σ-p_2 plane.

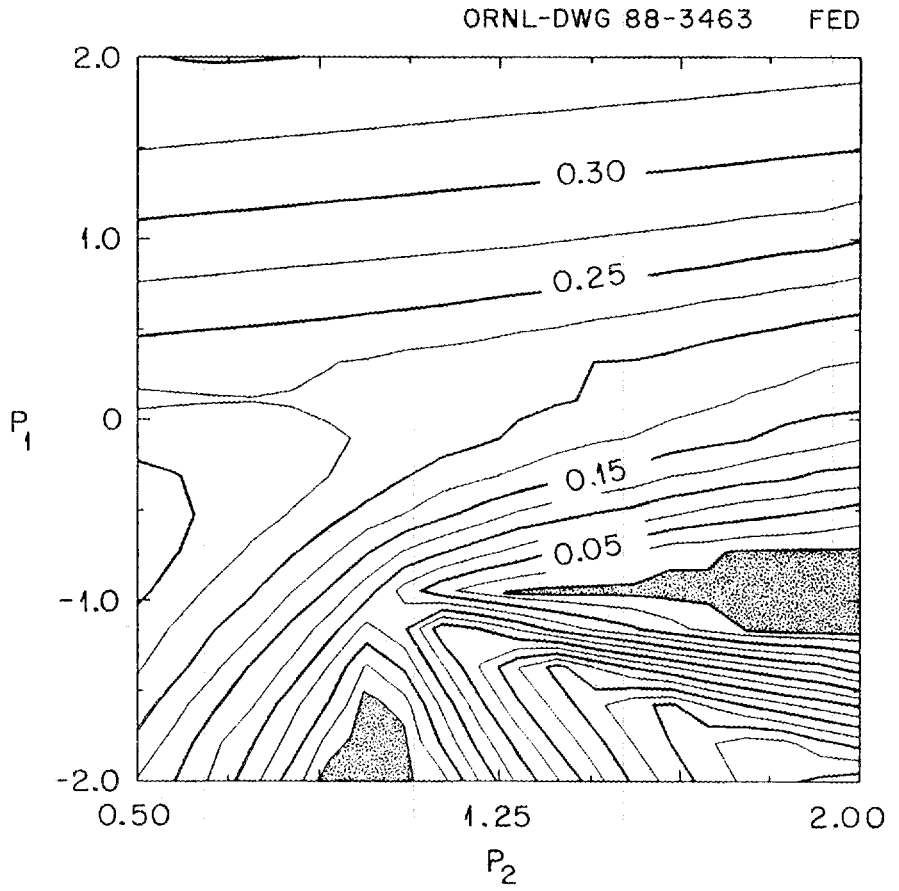

Fig. 14. Contours of constant alpha-particle losses in the p_1-p_2 plane.

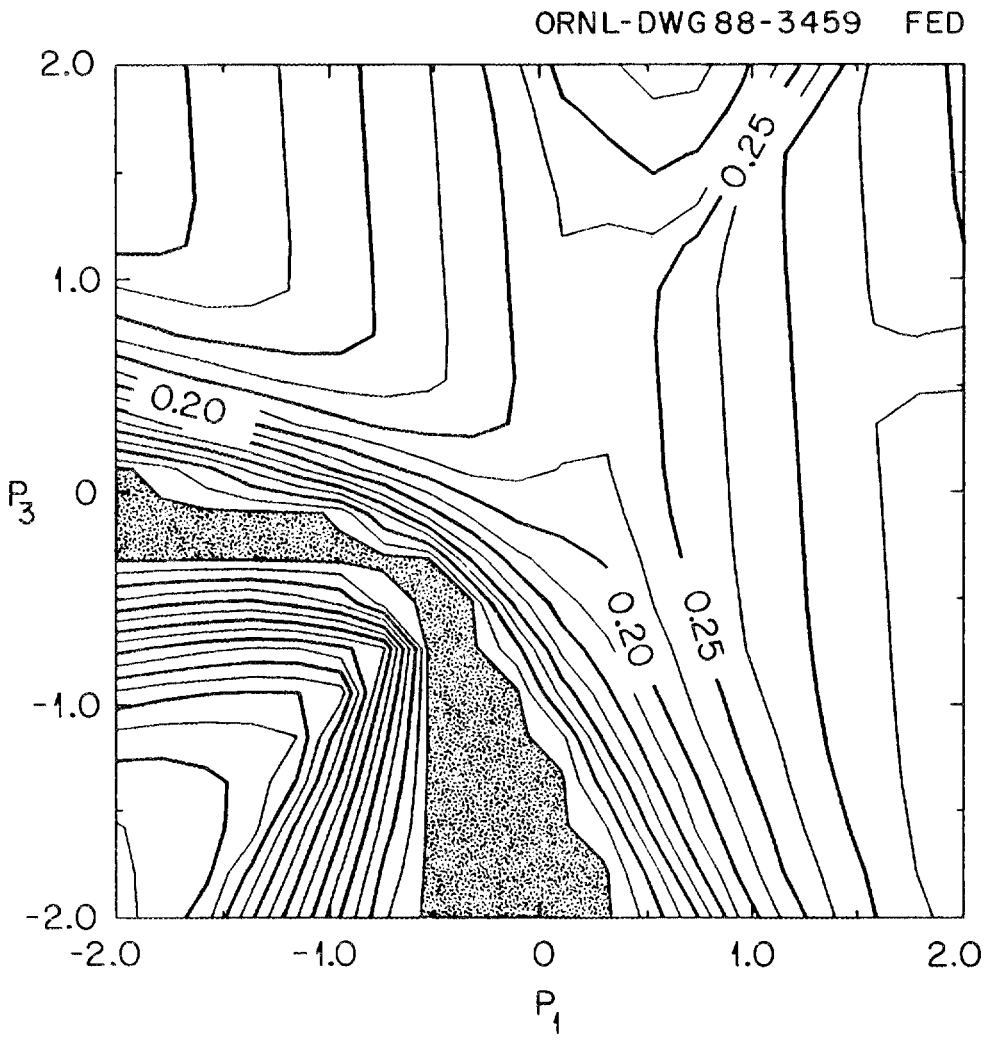

Fig. 15. Contours of constant alpha-particle losses in the p_3-p_1 plane.

losses extends to the left for $p_1 < 0$ and $p_3 \simeq 0$ and downward for $p_3 < 0$ and $p_1 \simeq 0$. Maximum losses occur for $p_3 \simeq 0.75$ and $p_1 \simeq 0.25$.

The relative insensitivity of alpha-particle losses to δ (and hence to B and $\bar{a}$) for configurations with large losses of trapped particles must be reexamined for configurations with reduced losses. The fraction of trapped particles born near the plasma center that are lost changes only from 47% to 53% as δ changes from 0.02 to 0.04 (corresponding to the change from a reactor with $R = 8$ m to a D-T burner with $R = 4$ m) for the base CT12 configuration. In contrast, for the CT12I configuration this fraction changes from 0 to 30% as δ changes from 0.02 to 0.04. The requirements on reduction of alpha-particle losses will be more stringent for smaller D-T burners than for reactors.

Model configurations are studied here in order to understand how the B spectra of compact torsatron configurations can be changed to improve alpha-particle confinement. However, flux surfaces are not guaranteed to exist for these model B spectra. Also, B spectra from practical coil sets usually contain higher-order ripple terms created by nonlinear beating between the primary ripple terms. The sensitivity of the results presented here to these higher-order terms should be addressed. Also, nonzero plasma beta effects may be important,[6] particularly for configurations with reduced losses of trapped particles. Although there is a relatively small change in the constant-B contours, nonzero beta causes a relatively large shift in the position of the flux surfaces relative to the constant-B contours; hence, $f_>$ could change. Although more work needs to be done, the results presented here are useful for understanding the trade-offs available in the design of torsatron reactors.

The fact that the direct alpha-particle losses can be made zero for configurations with low aspect ratio ($A = 5$) and large helical ripple ($p_2 = 1$–2) under a variety of conditions is very encouraging, in that it suggests that the relatively large direct losses found here are a consequence of the particular coil sets studied and not an inherent property of low-aspect-ratio configurations. The challenge will be to realize this potential reduction of alpha-particle losses in combination with good transport and high beta and with a coil geometry that is attractive for a reactor.

ACKNOWLEDGMENTS

The authors thank C. L. Hedrick and B. A. Carreras for suggesting the correlation between alpha-particle losses and the fractional area of closed B_{min} contours and the addition of $\ell = 1$ and $\ell = 3$ components to the field. They also acknowledge

V. E. Lynch for providing Fourier components of B for the configurations studied and R. H. Fowler for providing the orbit-following code. One author (SLP) also thanks P. N. Stevens for general guidance.

APPENDIX

The indirect loss of alpha particles due to scattering into the loss region is described by the Fokker-Planck equation given on each flux surface by[17,18]

$$\frac{1}{\tau_s v^2}\frac{\partial}{\partial v}\left[(v^3+v_c^3)f\right] - \frac{\alpha v_c^3}{\tau_s v^3}\frac{\partial}{\partial \xi}\left[(1-\xi^2)\frac{\partial f}{\partial v}\right] = S \ , \qquad \text{(A1)}$$

where $f(v,\xi)$ is the alpha-particle distribution function, $\xi = |v_\parallel/v|$, and the source function S can be assumed to be monoenergetic and isotropic in velocity space. The slowing-down time τ_s is defined by

$$\frac{1}{\tau_s} \equiv \frac{4\sqrt{2\pi}}{3}\,\frac{\sqrt{m_e}}{m_\alpha}\,\frac{e^4 n_e \ln\Lambda}{T_e^{3/2}} \ ,$$

where m_e and m_α are the electron and alpha-particle masses, e is the electron charge, n_e and T_e are the electron density and temperature, and $\ln\Lambda$ is the Coulomb logarithm. The critical velocity v_c at which electrons and ions contribute equally to the slowing down of the alpha particles is given by

$$v_c^3 \equiv \frac{3\sqrt{\pi}}{4}\,\frac{m_e}{m_p}\,[Z]\,v_e^3 \ ,$$

where v_e is the electron thermal velocity and m_p is the proton mass. The parameter α is related to the effective charge by $\alpha \equiv Z_{eff}/2A[Z]$, where $[Z] = \left[\sum_i Z_i^2 n_i (m_p/m_i)\right]/n_e$, $Z_{eff} = (1/n_e)\sum_i n_i Z_i^2$, and A is the atomic mass. The summations are over the different background plasma ion species. If $Z_{eff} = 1.5$ due to oxygen impurity and $T_e = 10$ keV, then $\alpha = 0.46$ and $W_{crit} = 330$ keV, where W_{crit} is the energy corresponding to v_c.

Equation (A1) has a simpler form,[17,19]

$$\frac{\partial g}{\partial t} = \alpha\frac{\partial}{\partial \xi}\left[(1-\xi^2)\frac{\partial g}{\partial \xi}\right] \ , \qquad \text{(A2)}$$

where

$$g = (v^3+v_c^3)f \ ,$$

$$t = \frac{1}{3}\ln\left(\frac{1+v_c^3/v^3}{1+v_c^3/v_f^3}\right) \ ,$$

and v_f is the velocity of 3.5-MeV alpha particles. The source function has been replaced by an equivalent initial condition $g(\xi,0) = 1$ for $\xi_c < \xi \leq 1$, and the boundary conditions are $g(\xi_c,t) = 0$ and $\partial g/\partial\xi(1,t) = 0$ for $t > 0$. The fraction of alpha particles lost between v_f and v because of scattering into the loss region is

$$P(v) = \alpha(1-\xi_c^2)\int_0^t \frac{\partial g}{\partial \xi}(\xi_c,t')dt'. \tag{A3}$$

The fraction of alpha-particle power lost is

$$Q(v) = \alpha(1-\xi_c^2)\int_0^t \frac{v^2(t')}{v_f^2}\frac{\partial g}{\partial \xi}(\xi_c,t')dt' \ . \tag{A4}$$

This form for the indirect losses simplifies their evaluation, since standard numerical routines are available for solving equations with the form of Eq. (A2).

Anderson et al. have solved Eq. (A2) analytically for $\xi_c = 0$ by using an integral approximation method, which is easily extended to treat loss regions of finite width ($\xi_c > 0$). We assume that the ξ variation of g is given by a trial function with undetermined coefficients that are functions of t. The coefficients are determined from moments of Eq. (A2). Anderson et al. take

$$\begin{aligned} g(\xi,t) &= \frac{3}{2}\frac{\xi}{w(t)} - \frac{1}{2}\left[\frac{\xi}{w(t)}\right]^3 , && 0 \leq \xi \leq w,\ t < t_{cr} \ , \\ &= 1 \ , && w \leq \xi \leq 1,\ t < t_{cr} \ , \\ &= a(t) + b(t)\xi^3 \ , && t \geq t_{cr} \ , \end{aligned}$$

where $t_{cr} = 1/8\alpha^2$. We take the same form for high energy,

$$\begin{aligned} g(y,t) &= \frac{3}{2}\frac{y}{w(t)} - \frac{1}{2}\left[\frac{y}{w(t)}\right]^3 , && 0 \leq y \leq w,\ t < t^* \ , \\ &= 1 \ , && w \leq y \leq 1,\ t < t^* \ , \end{aligned}$$

where $y = (\xi - \xi_c)/(1-\xi_c)$ and $t^* = t_{cr}(1-\xi_c)/(1+\xi_c)$, but we pick a simpler form at low energy,

$$g(y,t) = (3y - y^3)b(t) \ , \quad t > t^*.$$

The functions $w(t)$ and $b(t)$ are determined from the zeroth moment of Eq. (A2),

$$\frac{\partial}{\partial t}\int_{\xi_c}^1 g(\xi,t)d\xi = -\alpha^2(1-\xi_c^2)\frac{\partial g}{\partial \xi}(\xi_c,t) \ ,$$

yielding

$$P(v) = \left[\frac{9\alpha}{8}(1-\xi_c^2)t\right]^{1/2} , \qquad v \geq v^* ,$$
$$= (1-\xi_c)\left(1 - 0.844e^{3ct}\right) , \qquad v \leq v^* , \tag{A5}$$

and

$$Q(v) = \frac{3}{4\sqrt{2}}\frac{[\alpha(1-\xi_c^2)]^{1/2}}{v_f^2}\int_0^t \frac{v^2(t')}{\sqrt{t'}}dt' , \qquad v \geq v^* ,$$
$$= Q(v^*) + 2.02\alpha\frac{v_c^2}{v_f^2}(1+\xi_c)\left(1+\frac{v_c^3}{v_f^3}\right)^c \int_{v_c/v^*}^{v_c/v}[1+u^3]^{1+c}\,du , \qquad v \leq v^* , \tag{A6}$$

where $c = (4/5)\alpha(1+\xi_c)/(1-\xi_c)$ and v^* is the velocity corresponding to t^*. Equations (A5) and (A6) are shown as dot-and-dash lines in Fig. 8 vs the alpha-particle energy $W = \frac{1}{2}mv^2$. These equations reduce to the solution of Anderson et al. for $\xi_c = 0$, $v > v_{cr}$.

REFERENCES

1. B. A. CARRERAS, N. DOMINGUEZ, L. GARCIA, V. E. LYNCH, J. F. LYON, J. R. CARY, J. D. HANSON, and A. P. NAVARRO, "Low-Aspect-Ratio Torsatron Configurations," *Nucl. Fusion*, **28**, 1195 (1988); see also ORNL/TM-10030, Oak Ridge National Laboratory (1987).

2. J. F. LYON, B. A. CARRERAS, V. E. LYNCH, J. S. TOLLIVER, and I. N. SVIATOSLAVSKY, "Compact Torsatron Reactors," *Fusion Technol.*, accepted for publication; see also ORNL/TM-10572, Oak Ridge National Laboratory (May 1988).

3. T. MATSUI, H. NAKASHIMA, M. OHTA, et al., "Nuclear Design of a Heliotron-H Fusion Power Reactor," *J. Fusion Energy*, **4**, 45 (1985).

4. G. GRIEGER, E. HARMEYER, J. KISSLINGER, F. RAU, and H. WOBIG, "Advanced Stellarator Reactor and Burner Studies," in *Fusion Reactor Design and Technology (Proc. 4th IAEA Tech. Committee Mtg.)*, Yalta, 1986, Vol. 1, p. 341, International Atomic Energy Agency, Vienna (1986).

5. H. E. MYNICK and W. N. G. HITCHON, "Effect of the Ambipolar Potential on Stellarator Confinement," *Nucl. Fusion*, **23**, 1053 (1983).

6. R. H. FOWLER, J. A. ROME, and J. F. LYON, "Monte-Carlo Studies of Transport in Stellarators," *Phys. Fluids*, **28**, 338 (1985).

7. L. M. HIVELY, "Problems in Modeling Toroidal Field Ripple Loss of Alphas from a Tokamak Reactor," *Fusion Technol.*, **13**, 438 (1988).

8. D. D-M. HO and R. M. KULSRUD, "Alpha-Particle Confinement and Helium Ash Accumulation in Stellarator Reactors," *Plasma Phys. Controlled Fusion*, **28**, 781 (1986).

9. M. WAKATANI, S. KODAMA, M. NAKASUGA, and K. HANATANI, "Velocity-Space Loss Regions in Toroidal Helical Systems," *Nucl. Fusion*, **21**, 175 (1981).

10. H. E. MYNICK, "Improved Theory of Collisionless Particle Motion in Stellarators," *Phys. Fluids*, **26**, 1008 (1983).

11. C. L. HEDRICK, J. R. CARY, and J. S. TOLLIVER, "Adiabatic and Full Guiding-Center Motion in 3-D Toroidal Systems," submitted to *Phys. Fluids*.

12. J. F. LYON, B. A. CARRERAS, K. K. CHIPLEY, M. J. COLE, J. H. HARRIS, T. C. JERNIGAN, R. L. JOHNSON, V. E. LYNCH, B. E. NELSON, J. A. ROME, J. SHEFFIELD, and P. B. THOMPSON, "The Advanced Toroidal Facility," *Fusion Technol.*, **10**, 179 (1986).

13. A. H. BOOZER, "Guiding Center Drift Equations," *Phys. Fluids*, **23**, 904 (1980).

14. G. KUO-PETRAVIC, A. H. BOOZER, J. A. ROME, and R. H. FOWLER, "Numerical Evaluation of Magnetic Coordinates for Particle Transport Studies in Asymmetric Plasmas," *J. Comput. Phys.*, **51**, 261 (1983).

15. A. H. BOOZER and G. KUO-PETRAVIC, "Monte Carlo Evaluation of Transport Coefficients," *Phys. Fluids*, **24**, 851 (1981).

16. R. J. GOLDSTON, R. B. WHITE, and A. H. BOOZER, "Confinement of High-Energy Trapped Particles in Tokamaks," *Phys. Rev. Lett.*, **47**, 647 (1981).

17. J. G. CORDEY and W. G. F. CORE, "Energetic Particle Distribution in a Toroidal Plasma with Neutral Injection Heating," *Phys. Fluids*, **17**, 1626 (1974).

18. J. A. ROME, D. G. McALEES, J. D. CALLEN, and R. H. FOWLER, "Particle-Orbit Loss Regions and Their Effects on Neutral-Injection Heating in Tokamaks," *Nucl. Fusion*, **16**, 55 (1976).

19. D. ANDERSON, H. HAMNÉN, and M. LISAK, "α-Particle Ripple Losses During Slow Down in a Tokamak Reactor," *Phys. Fluids*, **25**, 353 (1982).

20. W. A. HOULBERG, S. E. ATTENBERGER, and L. M. HIVELY, "Contour Analysis of Fusion Reactor Plasma Performance," *Nucl. Fusion*, **22**, 935 (1982).

21. H. E. MYNICK, T. K. CHU, and A. H. BOOZER, "Class of Model Stellarator Fields with Enhanced Confinement," *Phys. Rev. Lett.*, **48**, 322 (1982).

22. F. MEYER and H. U. SCHMIDT, "Torusartige Plasmakonfigurationen Ohne Gesamtstrom Durch Ihren Querschnitt Im Gleichgewicht Mit Zinem Magnetfeld," *Z. Naturforsch.*, **13a**, 1005 (1958).

ORNL/TM-10792
Dist. Category UC-421, 424, 426, 427

INTERNAL DISTRIBUTION

1. L. A. Berry
2. B. A. Carreras
3. R. A. Dory
4. J. L. Dunlap
5. R. H. Fowler
6. J. H. Harris
7. H. H. Haselton
8. C. L. Hedrick
9. S. P. Hirshman
10. R. C. Isler
11. T. C. Jernigan
12. M. S. Lubell
13–16. J. F. Lyon
17. P. K. Mioduszewski
18. M. Murakami
19. G. H. Neilson
20–23. S. L. Painter
24. Y-K. M. Peng
25. J. A. Rome
26. M. J. Saltmarsh
27. T. E. Shannon
28. J. Sheffield
29. P. N. Stevens
30. D. W. Swain
31. P. B. Thompson
32–33. Laboratory Records Department
34. Laboratory Records, ORNL-RC
35. Document Reference Section
36. Central Research Library
37. Fusion Energy Division Library
38–39. Fusion Energy Division Publications Office
40. ORNL Patent Office

EXTERNAL DISTRIBUTION

41. Office of the Assistant Manager for Energy Research and Development, U.S. Department of Energy, Oak Ridge Operations Office, P. O. Box E, Oak Ridge, TN 37831
42. J. D. Callen, Department of Nuclear Engineering, University of Wisconsin, Madison, WI 53706-1687
43. J. F. Clarke, Director, Office of Fusion Energy, Office of Energy Research, ER-50 Germantown, U.S. Department of Energy, Washington, DC 20545
44. R. W. Conn, Department of Chemical, Nuclear, and Thermal Engineering, University of California, Los Angeles, CA 90024
45. S. O. Dean, Fusion Power Associates, 2 Professional Drive, Suite 248, Gaithersburg, MD 20879
46. H. K. Forsen, Bechtel Group, Inc., Research Engineering, P. O. Box 3965, San Francisco, CA 94105

47. J. R. Gilleland, Lawrence Livermore National Laboratory, P.O. Box 5511, Livermore, CA 94550
48. R. W. Gould, Department of Applied Physics, California Institute of Technology, Pasadena, CA 91125
49. R. A. Gross, Plasma Research Laboratory, Columbia University, New York, NY 10027
50. D. M. Meade, Princeton Plasma Physics Laboratory, P.O. Box 451, Princeton, NJ 08544
51. M. Roberts, International Programs, Office of Fusion Energy, Office of Energy Research, ER-52 Germantown, U.S. Department of Energy, Washington, DC 20545
52. W. M. Stacey, School of Nuclear Engineering and Health Physics, Georgia Institute of Technology, Atlanta, GA 30332
53. D. Steiner, Nuclear Engineering Department, NES Building, Tibbetts Avenue, Rensselaer Polytechnic Institute, Troy, NY 12181
54. R. Varma, Physical Research Laboratory, Navrangpura, Ahmedabad 380009, India
55. Bibliothek, Max-Planck-Institut für Plasmaphysik, D-8046 Garching, Federal Republic of Germany
56. Bibliothek, Institut für Plasmaphysik, KFA, Postfach 1913, D-5170 Julich, Federal Republic of Germany
57. Bibliotheque, Centre de Recherches en Physique de Plasmas, 21 Avenue des Bains, 1007 Lausanne, Switzerland
58. F. Prevot, CEN/Cadarache, Departement de Recherches sur la Fusion Controlee, F-13108 Saint-Paul-lez-Durance, France
59. Bibliotheque, CEN/Cadarache, Departement de Recherches sur la Fusion Controlee, F-13108 Saint-Paul-lez-Durance, France
60. Library, Culham Laboratory, UKAEA, Abingdon, Oxfordshire, OX14 3DB, England
61. Library, FOM-Instituut voor Plasmafysica, Rijnhuizen, Edisonbaan 14, 3439 MN Nieuwegein, The Netherlands
62. Library, Institute of Plasma Physics, Nagoya University, Nagoya 464, Japan
63. Library, International Centre for Theoretical Physics, P.O. Box 586, I-34100 Trieste, Italy
64. Library, Laboratorio Gas Ionizatti, CP 56, I-00044 Frascati, Rome, Italy
65. Library, Plasma Physics Laboratory, Kyoto University, 611 Gokasho, Uji, Kyoto, Japan
66. Plasma Research Laboratory, Australian National University, P.O. Box 4, Canberra, A.C.T. 2000, Australia
67. Thermonuclear Library, Japan Atomic Energy Research Institute, Tokai Establishment, Tokai-mura, Naka-gun, Ibaraki-ken, Japan
68. G. A. Eliseev, I. V. Kurchatov Institute of Atomic Energy, P. O. Box 3402, 123182 Moscow, U.S.S.R.

69. V. A. Glukhikh, Scientific-Research Institute of Electro-Physical Apparatus, 188631 Leningrad, U.S.S.R.
70. I. Shpigel, Institute of General Physics, U.S.S.R. Academy of Sciences, Ulitsa Vavilova 38, Moscow, U.S.S.R.
71. D. D. Ryutov, Institute of Nuclear Physics, Siberian Branch of the Academy of Sciences of the U.S.S.R., Sovetskaya St. 5, 630090 Novosibirsk, U.S.S.R.
72. V. T. Tolok, Kharkov Physical-Technical Institute, Academical St. 1, 310108 Kharkov, U.S.S.R.
73. Library, Academia Sinica, P.O. Box 3908, Beijing, China (PRC)
74. R. A. Blanken, Experimental Plasma Research Branch, Division of Applied Plasma Physics, Office of Fusion Energy, Office of Energy Research, ER-542, Germantown, U.S. Department of Energy, Washington, DC 20545
75. K. Bol, Princeton Plasma Physics Laboratory, P.O. Box 451, Princeton, NJ 08544
76. R. A. E. Bolton, IREQ Hydro-Quebec Research Institute, 1800 Montee Ste.-Julie, Varennes, P.Q. JOL 2P0, Canada
77. D. H. Crandall, Experimental Plasma Research Branch, Division of Applied Plasma Physics, Office of Fusion Energy, Office of Energy Research, ER-542 Germantown, U.S. Department of Energy, Washington, DC 20545
78. R. L. Freeman, GA Technologies, Inc., P.O. Box 81608, San Diego, CA 92138
79. K. W. Gentle, RLM 11.222, Institute for Fusion Studies, University of Texas, Austin, TX 78712
80. R. J. Goldston, Princeton Plasma Physics Laboratory, P.O. Box 451, Princeton, NJ 08544
81. J. C. Hosea, Princeton Plasma Physics Laboratory, P.O. Box 451, Princeton, NJ 08544
82. S. W. Luke, Division of Confinement Systems, Office of Fusion Energy, Office of Energy Research, ER-55 Germantown, U.S. Department of Energy, Washington, DC 20545
83. E. Oktay, Division of Confinement Systems, Office of Fusion Energy, Office of Energy Research, ER-55 Germantown, U.S. Department of Energy, Washington, DC 20545
84. D. Overskei, GA Technologies, Inc., P.O. Box 81608, San Diego, CA 92138
85. R. R. Parker, Plasma Fusion Center, NW 16-288, Massachusetts Institute of Technology, Cambridge, MA 02139
86. W. L. Sadowski, Fusion Theory and Computer Services Branch, Division of Applied Plasma Physics, Office of Fusion Energy, Office of Energy Research, ER-541 Germantown, U.S. Department of Energy, Washington, DC 20545
87. J. W. Willis, Division of Confinement Systems, Office of Fusion Energy, Office of Energy Research, ER-55 Germantown, U.S. Department of Energy, Washington, DC 20545
88. A. P. Navarro, Division de Fusion, Asociacion EURATOM/CIEMAT, Avenida Complutense 22, E-28040 Madrid, Spain

89. Laboratory for Plasma and Fusion Studies, Department of Nuclear Engineering, Seoul National University, Shinrim-dong, Gwanak-ku, Seoul 151, Korea
90. J. L. Johnson, Plasma Physics Laboratory, Princeton University, P.O. Box 451, Princeton, NJ 08544
91. L. M. Kovrizhnykh, Institute of General Physics, U.S.S.R. Academy of Sciences, Ulitsa Vavilova 38, 117924 Moscow, U.S.S.R.
92. O. Motojima, Plasma Physics Laboratory, Kyoto University, 611 Gokasho, Uji, Kyoto, Japan
93. V. D. Shafranov, I. V. Kurchatov Institute of Atomic Energy, P.O. Box 3402, 123182 Moscow, U.S.S.R.
94. J. L. Shohet, Torsatron/Stellarator Laboratory, University of Wisconsin, Madison, WI 53706
95. H. Wobig, Max-Planck Institut fur Plasmaphysik, D-8046 Garching, Federal Republic of Germany
96. N. A. Davies, Office of Fusion Energy, Office of Energy Research, ER-51 Germantown, U.S. Department of Energy, Washington, DC 20545
97. W. F. Dove, Office of Fusion Energy, Office of Energy Research, ER-543 Germantown, U.S. Department of Energy, Washington, DC 20545
98. R. J. Dowling, Office of Fusion Energy, Office of Energy Research, ER-53 Germantown, U.S. Department of Energy, Washington, DC 20545
99. D. Markevitch, Office of Fusion Energy, Office of Energy Research, ER-55 Germantown, U.S. Department of Energy, Washington, DC 20545
100. D. B. Nelson, Office of Fusion Energy, Office of Energy Research, ER-54 Germantown, U.S. Department of Energy, Washington, DC 20545
101. T. K. Chu, Plasma Physics Laboratory, Princeton University, P.O. Box 451, Princeton, NJ 08544
102. H. Furth, Plasma Physics Laboratory, Princeton University, P.O. Box 451, Princeton, NJ 08544
103. P. Rutherford, Plasma Physics Laboratory, Princeton University, P.O. Box 451, Princeton, NJ 08544
104. W. Stodiek, Plasma Physics Laboratory, Princeton University, P.O. Box 451, Princeton, NJ 08544
105. G. Grieger, Max-Planck-Institut für Plasmaphysik, D-8046 Garching bei München, Federal Republic of Germany
106. F. Rau, Max-Planck-Institut für Plasmaphysik, D-8046 Garching bei München, Federal Republic of Germany
107. H. Renner, Max-Planck-Institut für Plasmaphysik, D-8046 Garching bei München, Federal Republic of Germany
108. A. Iiyoshi, Plasma Physics Laboratory, Kyoto University, 611 Gokasho, Uji, Kyoto, Japan
109. K. Uo, Plasma Physics Laboratory, Kyoto University, 611 Gokasho, Uji, Kyoto, Japan

110. M. Wakatani, Plasma Physics Laboratory, Kyoto University, 611 Gokasho, Uji, Kyoto, Japan
111. M. Fujiwara, Institute of Plasma Physics, Nagoya University, Nagoya 464, Japan
112. H. Ikegami, Institute of Plasma Physics, Nagoya University, Nagoya 464, Japan
113. T. Uchida, Institute of Plasma Physics, Nagoya University, Nagoya 464, Japan
114. O. Pavlichenko, Kharkov Physico-Technical Institute, 310108 Kharkov, U.S.S.R.
115. R. Davidson, Plasma Fusion Center, Massachusetts Institute of Technology, NW16-202, 167 Albany St., Cambridge, MA 02139
116. I. N. Sviatoslavsky, Fusion Technology Institute, 529 Engineering Research Building, University of Wisconsin, 1500 Johnson Drive, Madison, WI 53706-1687
117. D. T. Anderson, Torsatron/Stellarator Laboratory, 1420 Engineering Building, 1415 Johnson Drive, Madison, WI 53706
118. H. Weitzner, Courant University of Mathematical Sciences, New York University, 251 Mercer Street, New York, NY 10012
119. P. R. Garabedian, Courant University of Mathematical Sciences, New York University, 251 Mercer Street, New York, NY 10012
120. K. B. Kartashev, I. V. Kurchatov Institute of Atomic Energy, P.O. Box 3402, 123182 Moscow, U.S.S.R.
121. G. H. Miley, 216 Nuclear Engineering Laboratory, University of Illinois, 103 S. Goodwin Avenue, Urbana, IL 61801
122. D. G. Swanson, Department of Physics, Auburn University, College Street, Auburn, AL 36849
123. F. L. Ribe, 319 Benson Hall, BF 10, University of Washington, 1400 Northwest Campus Parkway, Seattle, WA 98195
124. R. K. Linford, Controlled Thermonuclear Research Division, Los Alamos National Laboratory, P.O. Box 1663, Los Alamos, NM 87545
125. T. K. Fowler, L-640, Lawrence Livermore National Laboratory, P.O. Box 5511, Livermore, CA 94550
126. D. E. Baldwin, L-640, Lawrence Livermore National Laboratory, P.O. Box 5511, Livermore, CA 94550
127. A. J. Wootton, Fusion Research Center, RLM 11.222, The University of Texas at Austin, Austin, TX 78712
128. H. L. Berk, Institute for Fusion Studies, RLM 11.222, The University of Texas at Austin, Austin, TX 78712
129. T. Ohkawa, Fusion and Advanced Technologies, GA Technologies, Inc., P.O. Box 85608, San Diego, CA 92138

130. S. M. Hamberger, Plasma Research Laboratory, Research School of Physical Sciences, Australian National University, P.O. Box 4, Canberra, A.C.T. 2600, Australia
131. A. H. Boozer, Physics Department, College of William and Mary, Williamsburg, VA 23185
132. Library, JET Joint Undertaking, Abingdon, Oxon OX14 3EA, England
133. Library, Japan Atomic Energy Research Institute, Naka, Japan
134. Bibliothek, Kernforschungszentrum Karlsruhe GmbH, Postfach 3640, D-7500 Karlsruhe 1, Federal Republic of Germany
135. T. C. Hender, Culham Laboratory, UKAEA, Abingdon, Oxfordshire, OX14 3DB, England
136. A. Grau Malonda, Division de Fusion, Asociacion EURATOM/CIEMAT, Avenida Complutense 22, E-28040 Madrid, Spain

137–196. Given distribution according to DOE/OSTI-4500, Magnetic Fusion Energy (Distribution Category UC-421, 424, 426, 427: Plasma Systems, Fusion Systems, Experimental Plasma Physics, Theoretical Plasma Physics)